Dark Matter Directionality:

Effect of Nuclear Recoil Direction Relative to Applied Electric Field on Ionization Yield in the LUX Detector

Nicholas Zachary Stern

Department of Physics

Brown University

A thesis submitted for the degree of

Bachelor of Science in Physics

May 2018

Acknowledgements

I'd like to extend a huge thank you to Professor Rick Gaitskell for his patience and guidance over the past two and a half years working for the LUX collaboration. You were instrumental in helping me get funding to fly out to Lead, SD and work as a part of the LUX team on site, which was an immense privilege and opportunity that I thoroughly enjoyed. Thank you to all of the graduate students and postdoctoral researchers in the research group, Casey Rhyne, Will Taylor, DQ Huang, Samuel Chan, and Junhui Lao for answering my many questions and helping me get simulation software working. You were always willing to help me out even when you were extremely busy yourselves. Thank you to Jake Lyle, Devon Seymour, and Connor Lynch for the late night laughs and company while working in the office, and for introducing me to Reddit. Thanks to Connor Flexman for tracking me down in the Brown University Bookstore and asking if I wanted to join the lab in the first place.

Thank you to Kara Hartig, Dara Storer, Zoe Canaras, Marlene Ortega, Cory Greer, Heesoo Kim, Jason Chan, Michelle Miller, Emily Yaruss, and many others for the years of homework help, company, and solidarity through the trials and tribulations of the physics curriculum.

Thank you to Professor Ian Dell'antonio for writing so many recommendation letters for me over the years, and for also being a great teacher and advisor!

Thank you to my family for allowing me the freedom and flexibility to pursue what I love and for the opportunity to attend Brown and become a part of such an amazing community.

Thank you to Alex Diehl for listening to me spout endlessly about bugs in my code and about physics in general. You've not only supported me, but helped me realize that even though I study the universe, there is a world outside of my own that continuously revolves no matter what happens on campus.

Abstract

There is substantial evidence to suggest that approximately 84% of the material in our universe is comprised of non-luminous matter called "dark matter." One promising candidate for dark matter is the Weakly Interacting Massive Particle (WIMP), a theoretical particle that interacts via gravity and a weak-like force. The Large Underground Xenon (LUX) experiment was an initiative to detect WIMP recoils using a liquid xenon scintillator placed deep underground. Due to the motion of the solar system through the Milky Way, WIMP's are expected to preferentially scatter along the axis of their incidence direction. As such, the ability to resolve the directionality of a recoil would be a powerful metric for discriminating WIMP recoils from terrestrial background. This thesis explores a potential method for resolving the axial direction of a recoil, using 107.2 live hours of nuclear recoil calibration data to try and identify any anisotropy in the ionization yield as a function of the angle between the xenon nuclear recoil track and the applied electric field in the LUX detector. The purported anisotropy would come from increased recombination emission in ionization tracks parallel to the electric field vs. perpendicular. The analysis results indicate no appreciable signal at the 95% confidence level. Therefore, any anisotropy would be beneath the sensitivity threshold achieved.

Contents

List of Figures

Chapter 1

Dark Matter

1.1 The Origin of Dark Matter

The universe is vast and exotic. It's both a desert and a jungle, juxtaposing vibrant swirls of stellar clusters and galaxies with swaths of interstellar darkness, stretching billions of light years in all directions. For as long as humans have walked the earth, we've studied the cosmos to try and understand our place within it. We've progressed from recording stellar motion with the naked eye to taking stunning deep field images from space with intricate telescopes that orbit Earth. From our direct observations we've developed detailed models that can explain how stars synthesize fuel to generate elements, how stellar clusters form and dissipate, and even how high energy radiation is jettisoned from extremely massive objects like neutron stars and black holes.

However, since the 1930's it has become increasingly apparent that direct observations alone cannot account for the physical behavior of some larger scale objects on the night sky. One of the first detected anomalies occurred in 1932 when Swiss astronomer Fritz Zwicky used galactic dynamics to estimate the mass of the Coma Galaxy Cluster.[1] To his surprise, Zwicky obtained a value 400 times larger than the expected mass contribution from luminous matter.[1] He therefore inferred that there must be non-luminous, or "dark" matter present to explain the discrepancy, placing his trust in the theory of gravity. Zwicky's postulate gave rise to the name "dark matter," and in the past 80 years there has been a wealth of evidence to substantiate the presence of this non-luminous matter. In fact, the most successful cosmological models to date rely on the existence of dark matter to create the large scale structure of the universe we see today.

[1] See Appendix A-1 for a more detailed discussion of how Zwicky estimated the mass of the cluster.

This chapter aims to provide context for understanding the motivation to search for dark matter by explaining the importance of such a discovery, walking through the leading theories for what comprises the missing mass, and then surveying some of the evidence for its existence.

1.2 Why Does it *Matter*?

The presence or absence of dark matter will not swing elections, save coral reefs, or lower the cost of a college education, but qualifying the nature of dark matter is so important that the first experiment to do so will most assuredly win a Nobel Prize in physics. This is in part because dark matter has become increasingly essential to explain the makeup and evolution of the universe, but also because, simply put, we believe there is a lot of it. Dispelling the mystery of dark matter would elucidate a substantial fraction of the cosmos.

We cannot discretize and count how much dark matter exists in the universe, so instead it is most useful to consider the ratio of dark matter to baryonic or, "normal" matter. In order to get a sense for how much baryonic matter is in the universe, we have to make two assumptions about the *large-scale* structure of the universe. The first assumption is that the universe is homogeneous, meaning there should be nothing special or unique about making observations from our general location vs. another arbitrary location in space. The second assumption is that the universe is isotropic, which means there should be no special directionality to the universe. These two assumptions are wrapped into a single idea called the Cosmological Principle, and allow us to extrapolate observations about a slice of the cosmos to the greater whole.[2] For example, we can count the number of galaxies in a representative sample of the sky and scale that number up to give an estimate for the total number of galaxies in our observable universe. Through this technique, current estimates infer that there are as many as 2 trillion galaxies or more beyond our own Milky Way![2] What's more, each galaxy could contain anywhere from 100 million to 100 billion stars, hot balls of gas which are individually so massive that they provide enough gravitational energy to induce nuclear fusion. Evidently there is an enormous amount of visible material in the universe, but these numbers still pale in comparison to the projected amount of dark matter that surrounds it.

[2]These assumptions have been substantiated by evidence from the CMB, which shall be discussed in more detail in the next section.

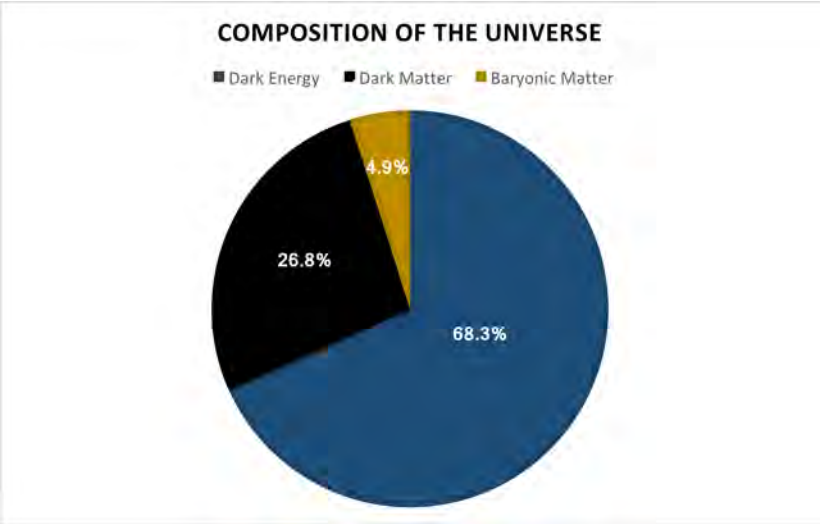

Figure 1.1: Chart outlining the composition of the universe according to the 2015 Planck Collaboration results.

In 2015 the Planck Collaboration published results from their study of the Cosmic Microwave Background (CMB), in which they provided refined estimates for the breakdown of energy in the universe, shown in Figure 1.1.[3] As pictured above, baryonic material comprises a meager 4.9% of the total energy density, dark matter 26.8%, and dark energy a whopping 68.3%![3] The Planck measurement reveals how much we have left to learn about the makeup of our world. All in all, according to the Planck results, more than 95% of the energy in our universe is unaccounted for, and there is over five times as much dark matter than baryonic matter.[4] Next, we shall dive deeper into understanding this result.

1.2.1 Baryonic Matter

As referenced previously, the term baryonic matter was used synonymously with "normal" matter. Examples of baryonic matter include kitchen tables, the sun, and all living organisms. The underlying connection between these objects is that they are built from atoms containing protons and neutrons. Protons and neutrons are two examples of subatomic particles called baryons, hence the term baryonic matter. This definition allows for a clear distinction between dark matter and objects such as far away planetary bodies or highly dispersed interstellar gas that could be considered

[3] An overview of the methodology behind obtaining these measurements will be presented in the next section.

[4] Note that mass can be represented as energy by converting through Einstein's famous formula, $E = mc^2$.

"dark" because we technically cannot see them. Unlike dark matter, the baryons that planets and gas clouds are built from do interact with light through various scattering, absorption, and reflection processes that would render them detectable by conventional means to a nearby observer. Their constituent atoms are well classified as a part of the periodic table of elements.

It is still unclear as to exactly how much baryonic material resides in galaxies and how much is spread across the interstellar medium in the form of gas. However, current estimates speculate that less than 10% of all baryonic matter is contained within galaxies, further contextualizing how much dark matter is present in the universe.[4]

1.2.2 Dark Energy

Looking at Figure 1.1, it is impossible to ignore that dark energy accounts for the majority of the energy in the universe. Compelling evidence for dark energy didn't appear until 1998, but the concept was originally introduced by Einstein in 1917 as an addendum to his theory of general relativity.[5] He called it called the "cosmological constant," denoted Λ. The purpose of the added constant was to counterbalance gravity and allow for a balanced, static universe (the purported state of the universe at the time). In 1929, however, Edwin Hubble (for whom the famous Hubble Telescope is named after) made several distance measurements using Cepheid variable stars, and discovered that galaxies farther away are receding faster. Hubble's work indicated that there was a linear relationship between recession velocity (v) and distance (d). This relationship today is called Hubble's Law and is summarized in Eq. 1.1 below:

$$v = H_0 d \tag{1.1}$$

The constant H_0 is called Hubble's constant, and the while the value of the constant has been explored and refined a lot since 1929, the linear relationship is still valid for shorter distance scales. Hubble's results were the first to imply that the universe is expanding, not static.[6] As a result, there was no longer a need for additional energy to counteract gravity, and most chose to neglect Λ in the gravitational field equations for general relativity. For the next 50 years, cosmology models advanced in stride with observational technology. With the advent of computers came gravitational simulations with a focus on testing how accurately cosmology models could create virtual structures that matched observation. By the 1980's, however, it was becoming increasingly apparent that there were several discrepancies between observational data and even the most advanced simulation results. In particular, models at the

time could not replicate large-scale galaxy clustering.[7] One solution that emerged was to re-introduce the cosmological constant in a modified theory of state called the Λ-CDM model, though there was still no definitive evidence to back it up.

Then, in 1998, results from Reiss et. al., a study similar to Hubble's work in 1929, demonstrated that objects very far away are receding at a rate that is higher than previously anticipated.[8] This was an indication that the universe is not only expanding, but is expanding at an increasing rate. Consequentially, an energy source beyond radiation and matter is necessary to propel space to accelerate outwards, and the Λ parameter, nicknamed dark energy, gained relevance once more. There are plenty of theories as to what contributes the energy represented by the cosmological constant. One prominent theory is that dark energy is a property of space itself, and arises from quantum fluctuations and annihilations in vacuum. Suffice it to say that dark energy is not fully understood, but comes from a temporally uniform energy source necessary to cause space to accelerate as it expands.

1.2.3 Dark Matter

As with dark energy, dark matter is not fully understood and there are several different ideas as to what form it could take. Below are four prominent theories that are actively debated and explored today:

1. **MACHO's**: MACHO stands for MAssive Compact Halo Object. Examples of these objects include black holes and neutron stars, baryonic material that exists undetected in regions surrounding galaxies and stars. While this may sound like a plausible explanation, there are several issues with the idea. First, if dark matter were baryonic, that would contradict the abundance of elements predicted by Big Bang nucleosynthesis. Additionally, astronomical searches should have uncovered more MACHO's through events like gravitational microlensing. On top of that, detailed analysis of the CMB suggests that dark matter only interacts gravitationally, and therefore must be non-baryonic in nature.[9]

2. **Axions**: Axions are a theoretical particle put forth in 1977 to solve a problem in the field of quantum chromodynamics called the strong Charge-Parity (CP) problem. Quantum chromodynamics is the branch of physics that studies the strong force that governs interactions between quarks and gluons, the force that holds atomic nuclei together.[5] In short, CP symmetry is the idea that if

[5]Protons and neutrons are made up of quarks. In fact, a baryon is defined as a 3 quark particle. Gluons are what "glue" quarks together.

a particle is replaced with its antiparticle (same mass, opposite charge), then the laws of physics should not change (C-symmetry), but the spatial coordinates should be flipped (P-symmetry). For example, an electron and a positron should accelerate at the same rate but in opposite directions when placed in an electric field. In reality, CP symmetry can be violated, a very important result that could explain the dominance of matter over antimatter that we see in our universe today. The CP problem arises from the fact that quantum chromodynamics does not seem to violate CP symmetry. Understanding exactly how the axion solves this problem is quite complicated, but suffice it to state that the theorized parameters for the axion coincide well with the necessary conditions for a dark matter candidate. Detecting axions experimentally would therefore knock out two birds with one stone, or so to speak.[10]

3. **Sterile Neutrinos**: Neutrinos are extremely light particles that only interact through the weak force and gravity. Sterile neutrinos are a theorized counterpart to Standard Model neutrinos, but differ in that they only interact gravitationally. This theory is motivated by the observation that standard model neutrinos only exhibit left-handed chirality. All particles have an intrinsic property called "spin." Neutrinos, as fermions, have two possible orientations for their spin: in the direction of motion or against the direction of motion. Left-handed chirality means that their spin is always aligned against the direction of motion. All other known fermions exhibit both forms of chirality, and therefore it is rational to postulate that sterile neutrinos might exist. Similar to the axion, the theoretical particle has projected properties that fall in line with the expected parameters for dark matter. One complication with this idea is that sterile neutrinos are expected to decay, producing X-rays that have not been observed for the expected mass range for dark matter.[11]

4. **WIMP's**: Weakly Interacting Massive Particles (WIMP's) comprise one of the most enticing explanations for dark matter. Similar to neutrinos, these theoretical particles do not have electromagnetic charge. Instead, they interact via gravity, and possibly through an alternate, unknown mechanism with a probability for interaction similar to that of the weak force. To understand why the WIMP model has such value, it is necessary to rewind to the very beginning of the universe.

Big Bang nucleosynthesis is the study of the formation of particles and elements very early in the universe, from the instant after the Big Bang to about a minute.

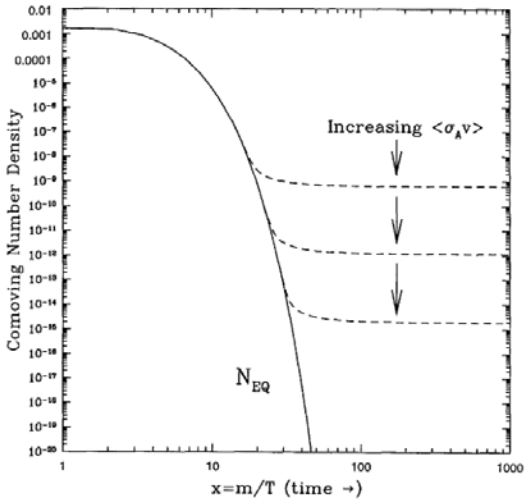

(a) Relationship between WIMP cross section for interaction and comoving number density. This shows that greater cross section leads to more annihilation and a lower number density at freeze out.[12]

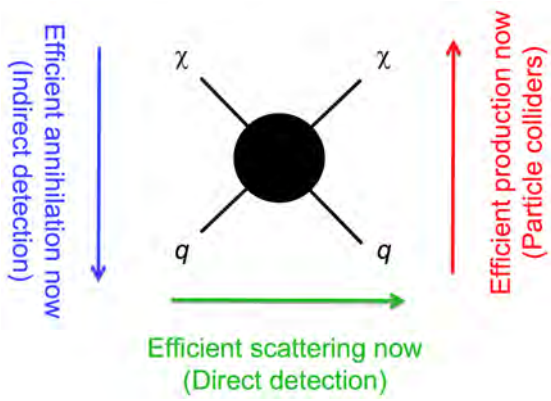

(b) Summary of the different types of WIMP interactions and methods to identify each one. In this subfigure, χ represents a WIMP particle and q represents a quark.[13]

Figure 1.2: WIMP freeze out and interaction diagrams.

The early universe was extremely hot and dense, which meant that particles were constantly interacting through various processes. In particular, when the thermal energy exceeded the mass energy of any given particle, these particle antiparticle pairs were created and destroyed in equilibrium. As the universe expanded it cooled. Once the thermal energy dropped below the mass energy, particle antiparticle pairs were no longer created, but continued to annihilate, exponentially decreasing in number density. The rate with which particles annihilate is dependent on their number density (n) and cross section (σ_A). Cross section is a physical parameter describing the probability with which an interaction process occurs, governed by subtle, small-scale physics and usually measured experimentally. As the universe expanded, the rate of annihilation decreased until it became insignificantly small, at a number density determined by the cross section. This cessation is known as "freeze out," and sets the abundance of the fundamental particles that exist in the universe today. The concept of freeze out is represented in Figure 1.2(a). Interestingly, if WIMP's self-annihilated through a mechanism similar to the weak-force, the corresponding cross section for annihilation would result in a WIMP abundance that is consistent with the mass density of dark matter we measure today! This is also known as the Wimp Miracle.

With the cross section for annihilation, and the expected relative velocity between

dark matter particles in a distribution at thermal equilibrium (v), we can solve for the expected number density of WIMP's at freeze out. Then, with the measured mass density of dark matter today (ρ), we can obtain the expected mass of a WIMP particle (m) through the relationships expressed in Eq. 1.2 and 1.3 below:

$$n \propto \frac{1}{< \sigma_A v >} \tag{1.2}$$

$$m = \frac{\rho}{n} \tag{1.3}$$

There is some uncertainty in the cross section for annihilation, and therefore the WIMP mass energy range that is actively explored spans anywhere from .01 GeV to 1000 GeV, depending on the source.

There are several approaches to verifying the existence of WIMP's. For one, dark matter annihilation could still occur in dense regions of the universe today, such as galactic centers. Byproducts from the annihilation, gamma rays for example, could be an indirect way of detecting WIMP's. There is also the possibility to create a WIMP-like particle from Standard Model particle collisions within particle accelerators. Particle collider experiments were vital in exploring the Super Symmetry (SUSY) theory, an additional motivator for the WIMP search. This model theorized that all fermions have ties to corresponding bosons, with the purpose of beautifying and connecting abstract mathematical formulas within the realm of particle physics. The low mass boson that is associated with the neutrino in the SUSY model, called the neutralino, would be a great candidate for dark matter.[14] Unfortunately, the Large Hadron Collider (LHC) in Switzerland has been searching for these partner bosons to no avail, casting doubt on the SUSY theory. Then there are direct detection experiments like the Large Underground Xenon (LUX) experiment, the focus of this thesis. LUX relies on the idea that if dark matter does interact via a mechanism similar to the weak force, then there is a cross section for dark matter to scatter off of standard nuclei. LUX operates under the pretense that one can pick up byproducts from such a scatter in the form of scintillation. These three ways in which dark matter may be detected (indirect detection, particle colliders, and direct detection) are outlined in the schematic shown in Figure 1.2(b).

To summarize, characterizing the source of the missing mass in the universe has spawned intricate theories and experiments that intersect both astrophysics and particle physics. Yet, how much evidence is there to substantiate the existence of dark matter beyond Fritz Zwicky's discovery in 1932? The next section will survey the most tenable evidence for dark matter that has arisen in the past century.

1.3 Evidence for Dark Matter

While the exact nature of dark matter might be mysterious, there is a wealth of evidence to establish it exists all around us. The following sections outline four distinct sources of evidence for dark matter.

1.3.1 Galaxy Rotation Curves

In disc-shaped galaxies like the Milky Way, luminous matter forms a plane, orbiting the galactic center with sporadic overdensities in the form of spiral arms that curl themselves around and around. Most of the luminous mass in these galaxies is located in the galactic bulge at the center, and the material in the disc orbits the central mass according to Newton's laws of gravity, just like Earth orbits the sun. At least this is what everyone thought, until Vera Rubin published a pivotal study in 1980 that pointed out a discrepancy between expected and observed rates of rotation in a survey of galactic discs.[15] According to Newton's law of gravity, expressed in Eq. 1.4, the force on any small star with mass m orbiting the galactic center of mass M will fall off with the square of the distance (r) between the two. Note that G is the universal gravitational constant.

$$F = \frac{GMm}{r^2} \tag{1.4}$$

Approximating the material in the disc as following circular orbits, we can invoke Newton's Second Law $F = ma$ and substitute in the centripetal acceleration, $a = v^2/r$. Setting the resultant expression equal to Eq. 1.4 and solving for velocity yields Eq. 1.5:

$$v = \sqrt{\frac{GM}{r}} \tag{1.5}$$

Thus, the velocity is expected to fall off as $1/\sqrt{r}$, but referencing Figure 1.3, observational evidence instead shows that the velocity does not decrease at all with distance from the galactic center. Instead, the galactic rotation curve appears to be flat.

This result has been corroborated from observing many different galaxies. Some theorized a form of modified Newtonian dynamics to explain the flat rotation curves, but the most accepted explanation is that there is additional, unseen mass distributed in a halo around these galaxies: dark matter. If the galaxy's mass were to increase

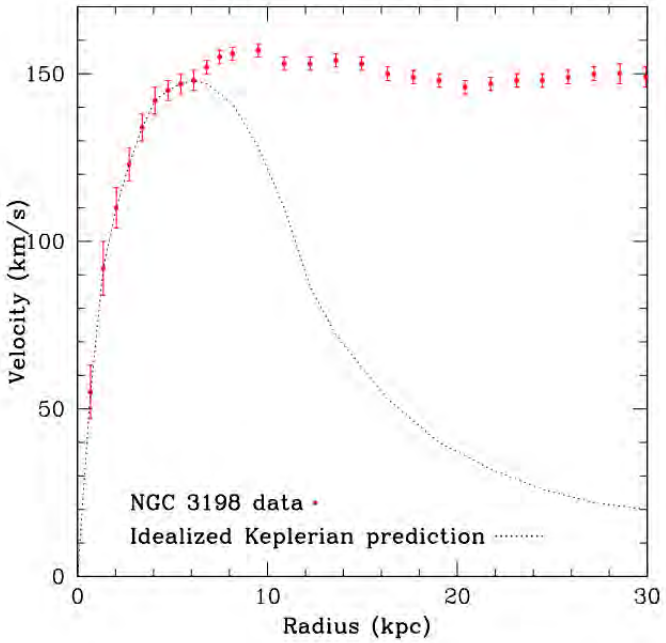

Figure 1.3: A depiction of the discrepancy between the expected and observed relationship between orbital velocity and distance from the galactic center.[16]

linearly as a function of radius, that would offset the radial dependence and generate the flat rotation curves that are observed.

1.3.2 Gravitational Lensing

Einstein's general relativity is a celebrated theory of gravity that expresses how massive objects distort the fabric of space like a bowling ball sitting on a foam mattress. We learn in secondary school that light always travels in a straight line until it impinges on another object. When the fabric of space is warped, however, the path of light gets warped with it, leading to distorted images of faraway objects. This is the phenomenon known as gravitational lensing. This effect was first theorized in the 1930's, and first observed in 1979 with the discovery of the Twin Quasar, a galactic nucleus that had its image replicated by a massive galaxy in the line of sight between the quasar and Earth.[17] Interestingly, the way in which light from distant sources is distorted reveals information about the mass of the lensing object. Therefore, gravitational lensing can be used to make a comparison between the mass calculated from the amount of luminous matter and the mass expected from severity of the distortion. As one might expect, there is a distinct discrepancy between the two measurements, providing more evidence that extra, unseen mass exists in galaxies. Figure 1.4 shows

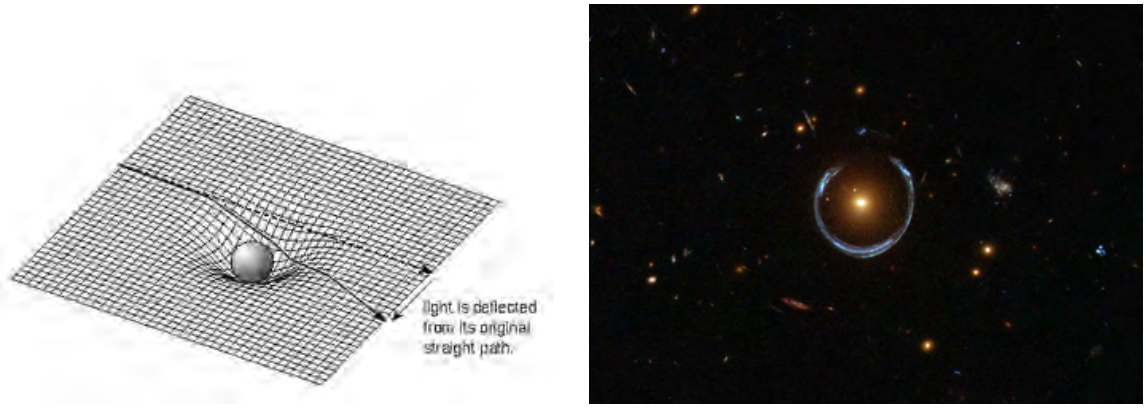

(a) Schematic demonstrating how massive objects can bend space and light.[18]

(b) Example of strong gravitational lensing. Light is distorted from a point source to a horseshoe shape.[19]

Figure 1.4: Gravitational lensing schematic and example.

a schematic of how space is stretched by massive objects as well as a real-life example of strong gravitational lensing.

1.3.3 Cosmic Microwave Background

As mentioned earlier in the discussion of freeze out, the early universe was incredibly hot and dense. Nanoseconds after the big bang, temperatures still exceeded 10^{14}K. It took approximately 10 microseconds for the universe to expand and cool to where quarks and gluons became bound into protons and neutrons, at temperatures of around 10^{12}K. 100 seconds after that, the universe had cooled to where protons and neutrons could bind together to create light nuclei, hydrogen and helium. However, the universe was still so hot and dense that electrons could not bind to nuclei before getting ripped off (ionized) once again by high energy photons. Photons could not travel very far before colliding with an electron, and for the next 300,000 years the universe existed as an opaque plasma of light nuclei. After this period of time had passed, the universe finally cooled to approximately 4000K, and the density became low enough for photons to travel unimpeded.[20] The photons that first escaped this primordial plasma and traveled for billions of year across the vast universe to reach our eyes today, constitute the Cosmic Microwave Background. The CMB is a bath of radiation coming from all directions, predicted in 1948 by Ralph Alpher and Robert Herman and then experimentally verified by Arno Penzias and Robert Wilson in 1964. The radiation has a blackbody temperature of 2.75K, which peaks in the microwave region of the electromagnetic spectrum.

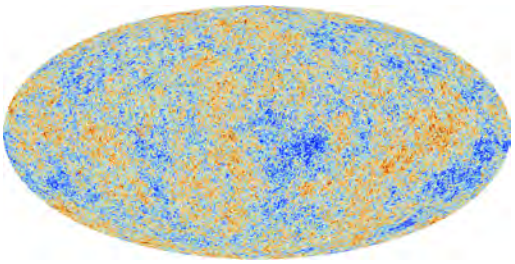

(a) The CMB as imaged by the Planck collaboration in 2013. Red/Blue spots represent higher than average/lower than average temperature.[21]

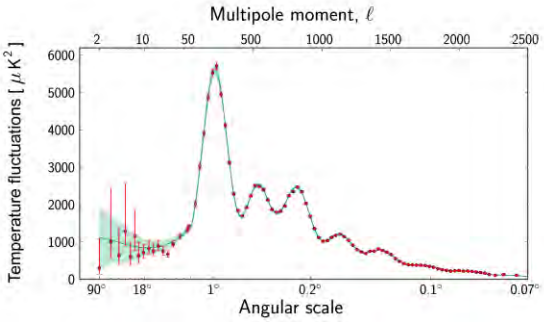

(b) The CMB power spectrum.[22]

Figure 1.5: The CMB and its power spectrum.

Depicted in Figure 1.5(a), the CMB was an immensely valuable discovery and has had a huge impact on modern cosmology. First and foremost, the CMB is critical evidence for the Big Bang, a singular explosion happening from a very smooth, concentrated source. Secondly, the CMB is largely uniform, which validates the Cosmological Principle, the assumption that the universe is homogeneous and isotropic, to a high degree. Third, by measuring temperature fluctuations at various angular scales, one can produce the power spectrum of the CMB, shown in Figure 1.5(b). This spectrum is packed with information about the mass distribution of the early universe, and contains enough information to fill a graduate level physics class. Fourth, analysis on the polarization of light from the CMB could provide evidence for cosmic inflation, a monumental theory about the expansion of the universe just moments after the Big Bang that could solve several mysteries in cosmology.[23][6]

The link between the light of last scattering and the mass distribution lies in the temperature fluctuations. The universe was dense enough so that matter was in thermal equilibrium and the gravitational field was very smooth, but overdense and underdense regions of mass still existed. Overdensities created gravitational potential wells, and photons escaping from these wells at the time of last scattering lost energy, resulting in the cold spots within the CMB. Likewise, hot spots in the CMB are from photons coming from regions where the mass density was lower. While the temperature fluctuations at face value give us a general picture of mass inhomogeneities, the

[6]Light, when considered a transverse wave, oscillates in a given planar orientation, called its polarization. Certain materials can filter light with a specific polarization, which is how some 3D glasses work.

distinction between baryonic matter and dark matter comes from a process known as baryon acoustic oscillations.

The key to understanding baryon acoustic oscillations comes from studying gravitational instability, or what happens when there are mass density fluctuations. For a given overdensity, gravity will pull matter together until the pressure builds up. Pressure in a gas is communicated at the speed of sound, c_s. If the time scale of gravitational collapse, t_g, is faster than the speed at which pressure can build (the speed of sound), the overdensity will continue to collapse under its own gravity. If, however, the time scale at which pressure builds is faster, then the matter will get pushed back out. This results in an oscillatory cycle of collapsing and rebounding. The determinant for these two eventualities is set by the Jeans length, λ_J, which is essentially the distance over which pressure can be communicated in the time of gravitational collapse. This relationship is expressed in Eq's 1.6 and 1.7 below:

$$\lambda_J = 2\pi c_s t_g \tag{1.6}$$

$$t_g = \frac{1}{2\pi}\left(\frac{\pi c^2}{G\bar{\epsilon}}\right)^{1/2} \tag{1.7}$$

At the time when photons were coupled to baryons in the dense plasma, radiation dominated the average energy density ($\bar{\epsilon}$) and set the scale of the Jeans length. Just before the time of last scattering, the Jean's length was approximately .6 Mpc, or 1.9x10^{22}m, much larger than the scale of the mass inhomogeneities. Therefore, pressure had the chance to build during collapse, and the overdensities oscillated at a frequency set by its size. This continued until the time of last scattering, when the baryons and photons separated. The baryon gas raised the average energy density and lowered the sound speed, decreasing the Jeans length scale dramatically. The speed of sound in the baryon gas was a factor of 2.5E-5 slower than in the gas of relativistic photons, and the Jeans length scale decreased to where the inhomogeneities stopped oscillating and began to collapse into the large scale structure we see today (i.e. galaxy clusters).[20] The peaks in the CMB power spectrum represent the density fluctuations that were at maximum compression or rarefaction at the time of last scattering. Note that the value on the Y axis can be considered an absolute value of the deviation from average temperature. The larger the angular scale, the larger the inhomogeneity and the slower the oscillation. Therefore, the first peak represents overdensities that just reached the first compression at the time of last scattering, the

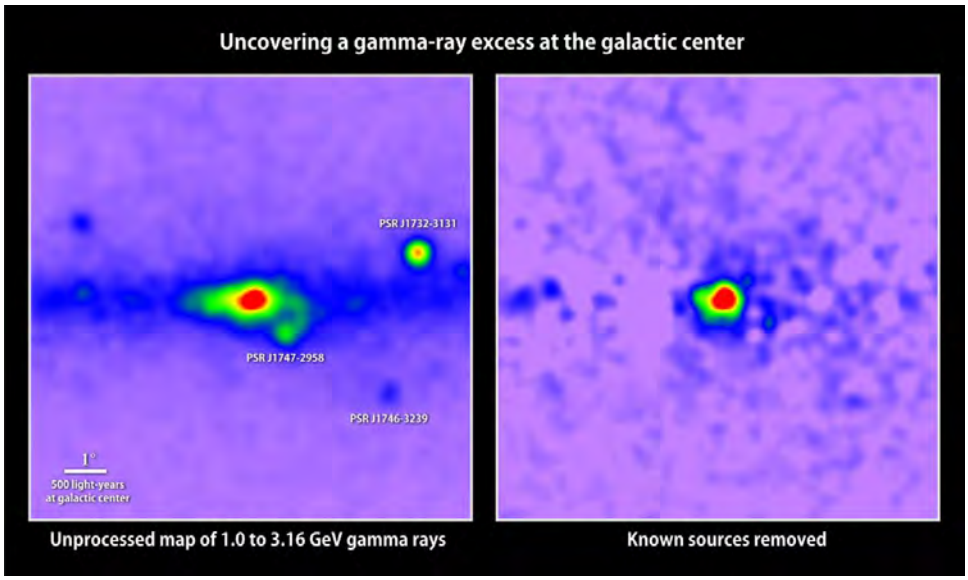

Figure 1.6: An image from Fermi-LAT demonstrating an excess of gamma ray radiation from the center of the galaxy.[24]

second peak represents higher frequency oscillations that reached the first rarefaction, the third peak represents the second compression, etc.

Now let us tie in how dark matter affects these acoustic oscillations. Recall that one of the fundamental properties of dark matter is that it does not interact electromagnetically. Therefore, it would not feel the radiation pressure that causes baryonic matter to rebound in the oscillatory cycle. As such, the presence of dark matter in the initial mass distribution serves to accentuate overdensities, since it adds to the infall but not the rebound. Without dark matter, the density perturbations would be a lot smaller, and we would not see the as much large scale structure as we do today. This is further evidence that dark matter is real, and not some miscalculation in Newtonian dynamics or baryonic matter that has been overlooked. Taking the ratio of the third to first peaks in the CMB power spectrum allows us to place bounds on the ratio of dark matter to the ratio of baryonic matter, resulting in the Planck percentages discussed earlier.

1.3.4 Gamma-Ray Excess/Dwarf Galaxies

Previously we mentioned that dark matter annihilation could occur today in overdense regions of the universe. The self-annihilation of dark matter would result in gamma ray radiation in a specific energy range corresponding to the expected mass range for WIMP's. One method for indirectly detecting dark matter is to isolate sources of

gamma rays in this energy range that cannot be explained by other, more conventional methods of production. Excitingly, in 2010 Dan Hooper and Lisa Goodenough published an analysis of data from the Fermi telescope, confirming the existence of an excess of gamma rays coming from the galactic center that is consistent with dark matter annihilation predictions. This gamma ray excess is shown in Figure 1.6.

However, an alternative explanation for this gamma ray energy has since emerged, stating that the radiation could also come from astronomical objects known as millisecond pulsars. Millisecond pulsars are examples of rapidly rotating neutron stars that emit a beam of high energy synchrotron emission out along its poles.[7] If the orientation of the neutron star is such that the the beam moves in and out of sight at a regular time period from our perspective, we see pulses of light, in this case on the order of milliseconds. Although this is a rational explanation for the gamma ray excess in the center of the galaxy, astronomical observations of milliseconds pulsars and their precursor, X-ray binary systems, indicate that there does not seem to be enough pulsars and binaries present to explain more than 10% of the excess gamma radiation.[25] This debate will likely be resolved in the next 10 years, with the advent of the astronomical technology to study the centers of nearby dwarf galaxies and resolve more millisecond pulsars within our own galaxy. Even so, the gamma ray excess observed could be evidence for the self-annihilation of dark matter in the center of the Milky Way.

[7] Synchrotron emission occurs when charged particles, such as electrons, spiral through a magnetic field.

Chapter 2

The LUX Experiment

The Large Underground Xenon (LUX) experiment was a direct detection dark matter experiment that ran from 2013 to 2016 at the Sanford Underground Research Facility (SURF) in Lead, South Dakota. The LUX detector, shown in Figure 2.2a, was a titanium cylinder filled with 370kg of cryogenically cooled liquid xenon located 4850ft below the surface in the Homestake Mine, the largest and deepest gold mine in North America until its closure in 2002. LUX operated in the Davis Cavern, the site made famous by Ray Davis, who was the first person to experimentally detect solar neutrinos in the late 1960's. The basic idea behind building LUX, as referenced in the previous chapter, was that dark matter can scatter elastically off of an atomic nucleus, producing an observable signal.

LUX set the record for the most sensitive direct dark matter detection experiment in the summer of 2016, after approximately 332 live days of data taking. The sensitivity, shown in Figure 2.1, is represented as a region in WIMP parameter space over which there is $> 90\%$ confidence that a WIMP would have been detected with those parameters. While LUX did not detect dark matter, it placed more stringent limits on the viable parameters for dark matter candidates, constraining theories and informing future experimentation.

This chapter begins with a description of the mechanics behind the generation and detection of signals within the LUX detector. We then survey the methods used to discriminate this signal from other activity in the detector, before introducing the topic of neutron calibration and linking that to the research question that guides the analysis in Chapter 3 of this thesis. Please note that for convenience, LUX will from now on be referred to in the present tense to provide the context in which the data analysis was performed.

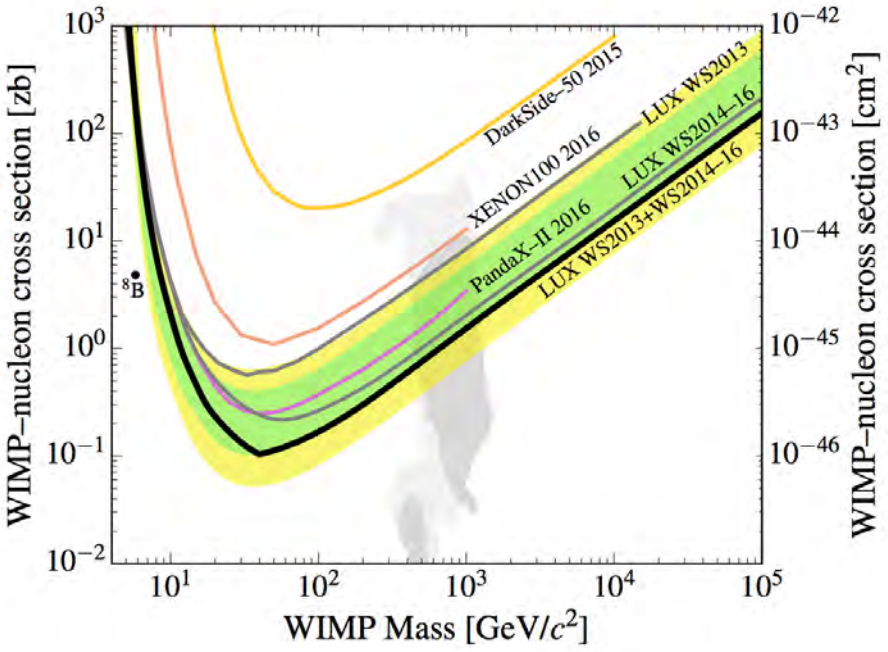

Figure 2.1: The 2016 LUX sensitivity results in WIMP parameter space, shown in black. The dark grey and light grey represent the 1-σ and 2-σ expectation regions for WIMP parameters favorbed by a SUSY model. Also shown here are sensitivity lines from PandaX-II, XENON100, and DarkSide-50 as of June 2016.[26]

2.1 Signals in LUX

2.1.1 Emission mechanisms

Collisional activity within LUX is picked up as scintillation released by liquid xenon when it gets struck. In dark matter direct detection experiments, there are several motivations for using liquid xenon as a target material. First and foremost, xenon has a large nucleus, which increases the probability of a scatter. Given the low expected cross section of dark matter, sizable nuclei are incredibly important.[1] Secondly, xenon has many stable isotopes, and does not radioactively decay at rates that interfere with signal detection. Third, xenon is transparent to its own scintillation, so that the intended signals will be allowed to propagate throughout the liquid xenon medium and get picked up by photomultiplier tube (PMT) arrays above and below the xenon volume. When an electromagnetically neutral particle collides elastically with a xenon nucleus (a nuclear recoil (NR)), the recoil energy catalyzes several emission generation mechanisms, ultimately converging to two types of signals, S1 and S2.

[1]In fact, the nomenclature for the "cross section" in particle physics stems from the physical representation of a sliced spherical particle. That's why bigger is better.

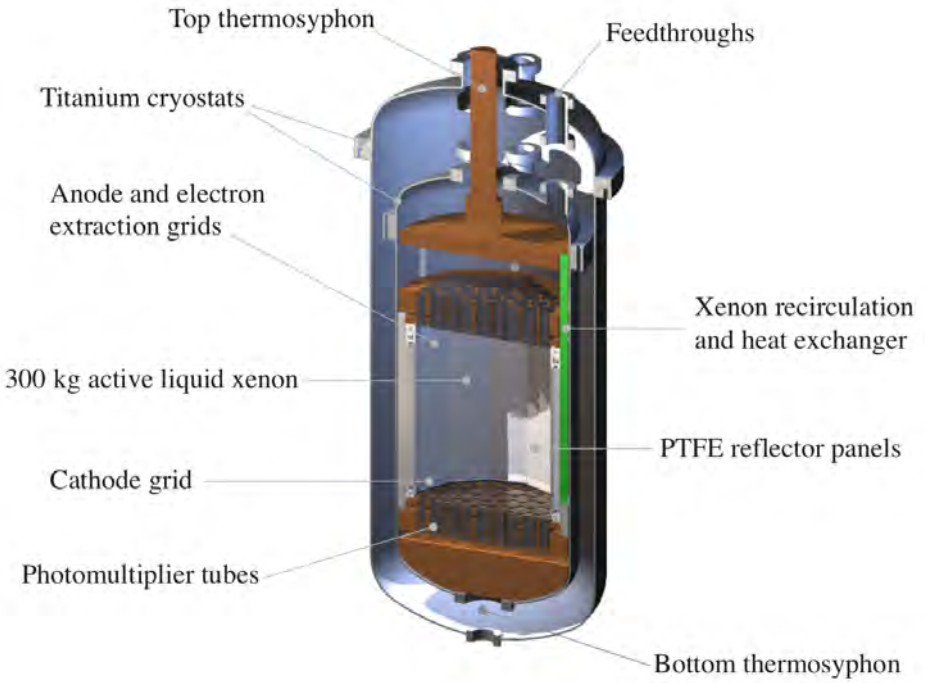

(a) Diagram of the internal LUX cryostat containing active Xe volume.

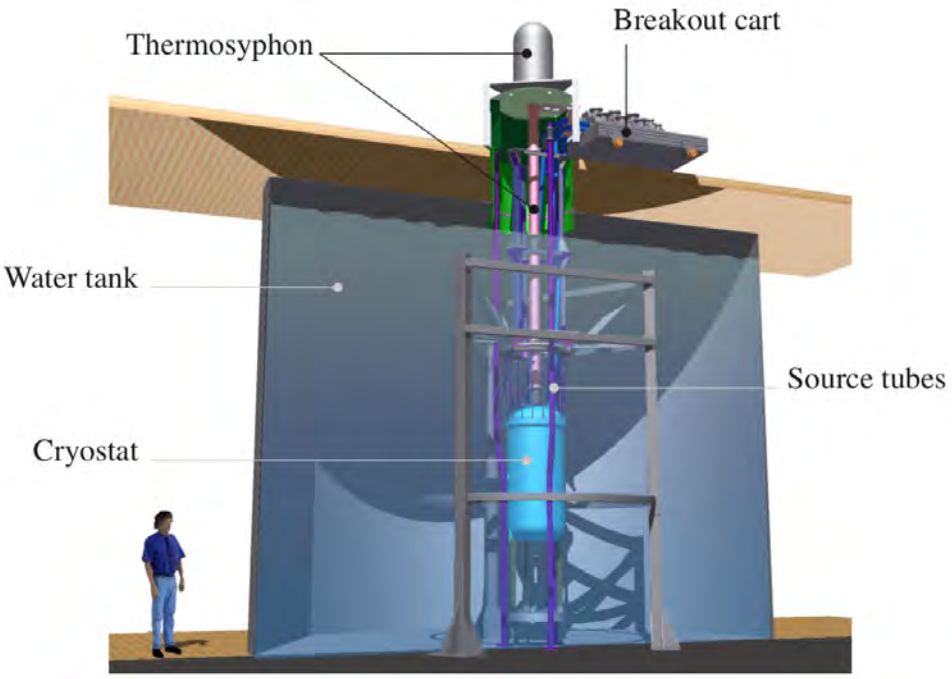

(b) Diagram of the external structure surrounding the cryostat.

Figure 2.2: Schematics of the LUX detector.[27]

When nuclear recoils occur, the recoil energy goes into exciting electrons to higher energy states within xenon atoms, creating Xe^*. The Xe^* atoms will then de-excite, producing photons (γ's) through the following process:

$$\begin{aligned} Xe^* + Xe &\rightarrow Xe_2^* \\ Xe_2^* &\rightarrow 2Xe + \gamma \end{aligned} \tag{2.1}$$

As indicated by Eq. 2.1, Xe^* atoms will join with a ground state xenon atom (Xe) to form Xe_2^*, an excited dimer. This dimer then de-excites by emitting a 175 nm photon and leaving behind two ground state xenon atoms. It is vital to characterize the time scale over which these signals appear and subside in order to determine whether these signals can be differentiated or not. In this signal generation process, Xe_2^* has two possible excitation states, the singlet and triplet states, that have characteristic relaxation times of 3.1 ns and 24 ns respectively. These timescales are too short for the two eventualities to be picked apart, and they both contribute to the same S1 pulse, which will be formally defined shortly.

Nuclear recoils can also ionize xenon, kicking off electrons (e^-) to create a positively charged Xe^+ ion. The freed electrons either get sucked up by LUX's electric field or recombine with other Xe^+ ions, eventually creating another excited Xe^* that generates more emission in the recombination process outlined below:

$$\begin{aligned} Xe^+ + Xe &\rightarrow Xe_2^+ \\ Xe_2^+ + e^- &\rightarrow Xe^{**} + Xe \\ Xe^{**} &\rightarrow Xe^* + \mathit{heat} \end{aligned} \tag{2.2}$$

This recombination process has a characteristic relaxation time of 45 ns. This time scale is too short to discriminate recombination photons from those generated in the process described by Eq. 2.1. Thus, the S1 signal is defined to be the joint photon emission from the processes outlined in Eq. 2.1 and 2.2. The S1 signal demarcates the beginning of a scattering event, even if the event includes multiple scatters. LUX is lined with PTFE reflector panels to maximize the efficiency of photon detection. Even still, individual photons are difficult to detect with high efficiency, and an important metric is the S1 detection efficiency or gain, denoted $g1$. For this analysis, $g1$ was calibrated to be $.115 \pm .004$, meaning approximately 11.5% of generated photons will be recorded.

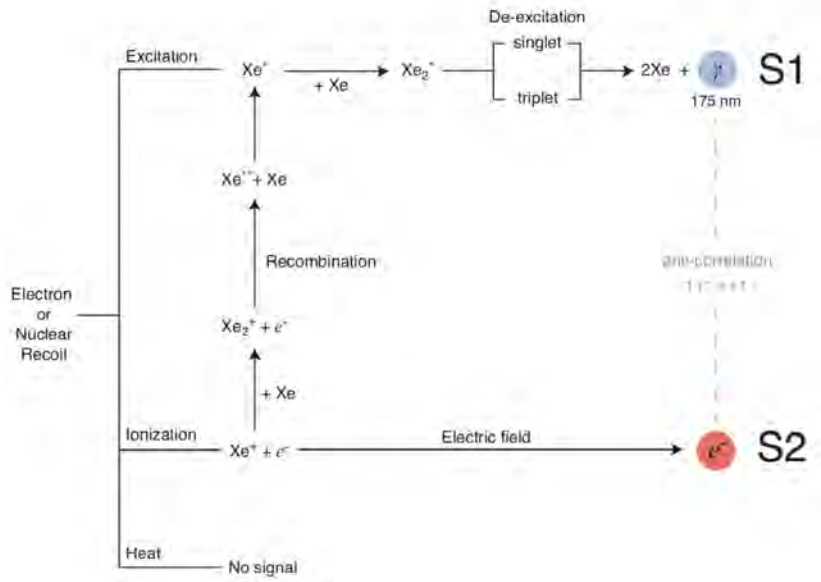

Figure 2.3: Summarization of the different Xe signal generation processes outlined by Eq. 2.1 and 2.2.[28]

The ionized electrons that escape the interaction site drift up in LUX's 180 V/cm applied electric field at a rate of 1.51 ± .01 mm/μs. Once the electrons reach the liquid surface they are extracted with an efficiency ($g2$) of .48 ± .04 into a gaseous xenon layer. In the gas layer they undergo electroluminescence, producing a second batch of photons referred to as S2. This secondary light yield was measured to be 23.77 ± .01 detected photons (phd) per ionized electron, and is typically much larger than the S1 signal. Figure 2.3 summarizes the different emission mechanisms that generate the S1 and S2 signals.

The time scale at which S2 signals reach the top PMT array are relatively longer than their corresponding S1 signals, with drift times stretching up to 324 μs. Given the constant rate at which electrons travel, the time between the S1 and S2 signals allows us to determine the depth at which the collision occurred. Furthermore, knowing the shape of the electric field and which PMT's saw the signal, one can constrain the x-y position of the scatter to within a centimeter. Therefore, the LUX detector is able to resolve when and where a nuclear recoil happened to great precision. These key points are represented in Figure 2.4 on the next page.

2.1.2 Detection Mechanisms

S1 and S2 signals in LUX are picked up by 122 Hamamatsu R8778 photomultiplier tubes split into a top and bottom array. Pictured in Figure 2.5a, these 5.7cm diam-

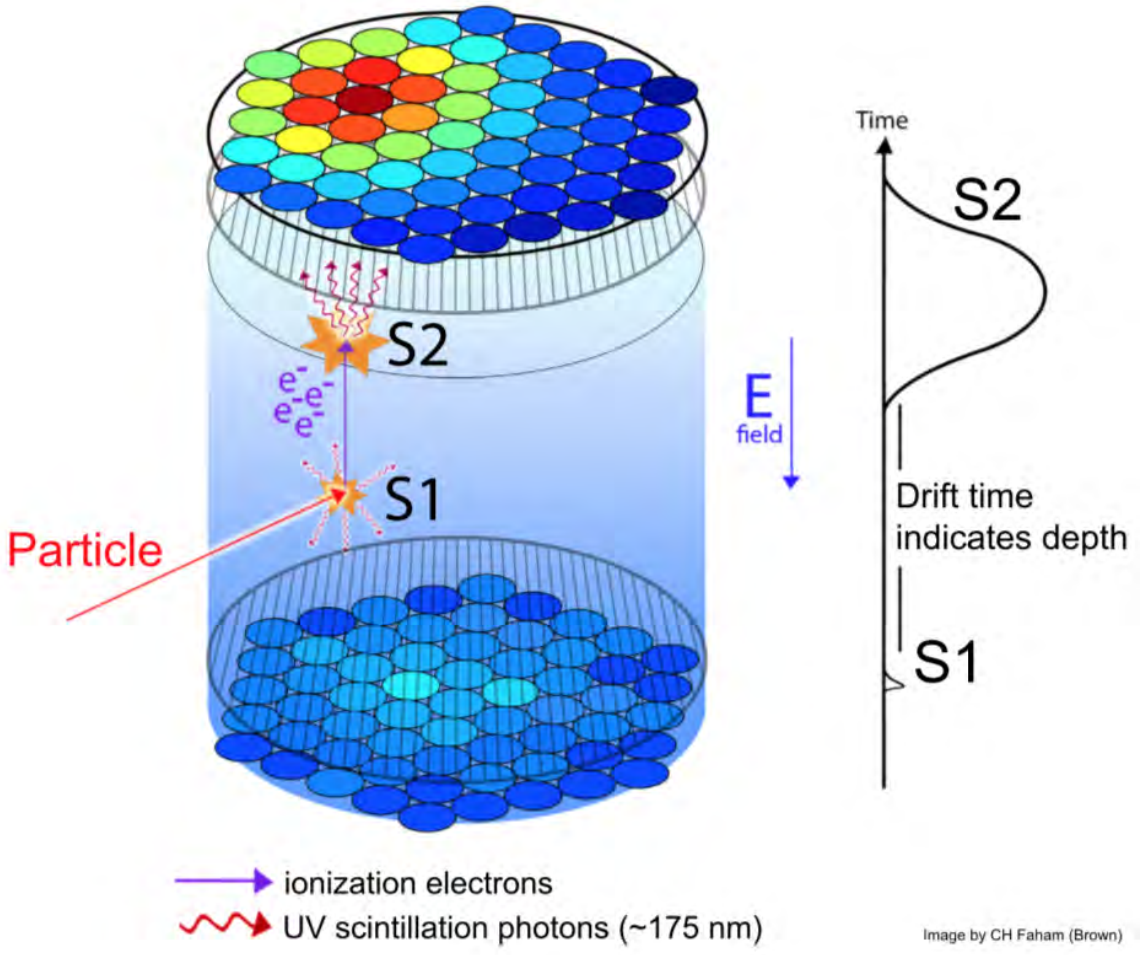

Figure 2.4: An overview of the S1, S2 signal detection process in LUX. A particle enters the liquid xenon volume and collides elastically with a xenon nucleus, producing S1 photons and ionizing electrons. The electrons then drift up and get extracted into the gas layer where they undergo electroluminescence, producing the second signal, S2. [28]

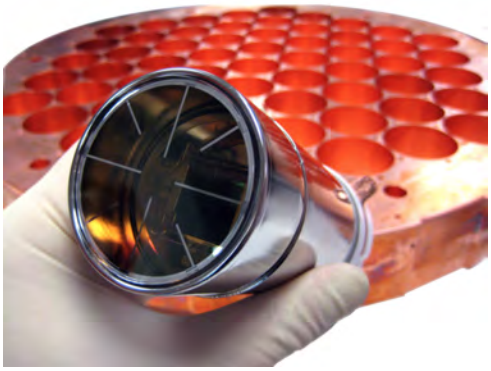

(a) Image of the Hamamatsu R8778 PMT. Behind it is the copper mounting structure for the PMT array.

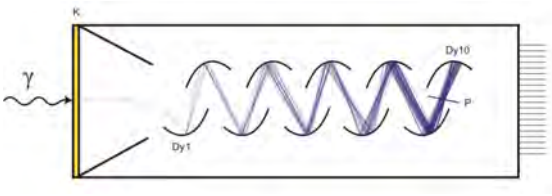

(b) Diagram of the amplification process within a PMT.

Figure 2.5: Image of the R8778 PMT and drawing of its internal operation mechanism.[28]

eter, cylindrical detection devices utilize the photoelectric effect to amplify a single photoelectron into a cascade of 10^5 to 10^7 electrons. The photoelectric effect occurs when an incoming photon causes an electron to be emitted from a material, referred to as a photoelectron (phe). Located within the glass housing of the front end of the R8778 PMT is the cathode, made from a mixture of rubidium, cesium, and antimony. Within the PMT is a series of 12 dynodes, slices of a secondary emissive material each connected to a pin on the back of the PMT. When operational, the pins are attached to a base with a step-wise electrical circuit of increasing resistance that creates a voltage gradient between each of the dynodes, generating an electric field in the direction of the cathode. As depicted in Figure 2.5b, an incoming photon will hit the cathode of the PMT and kick off a photoelectron that propagates down the electric field, crashing into each dynode and creating more photoelectrons in the process. In between the final two dynodes is the anode, a wire mesh that collects the charge and transmits the signal to the user for processing. The signal is digitized and recorded as a pulse of voltage.

PMT's are hardy, as they can operate at liquid xenon temperatures of 177K (-96^oC) and up to 5 atm of pressure. Even still, they occasionally break. In particular, PMT's can develop leaks that ruin the vacuum within. A compromised vacuum can cause increased activity within the PMT, obscuring external signals. One way to test for this is to immerse the PMT in complete darkness and measure the rate at which pulses above a certain threshold are received. This measurement is called the "dark rate," and PMT's with abnormally high dark rates never make it into the

LUX detector. Additionally, a poor PMT vacuum can lead to unwanted behavior called "afterpulsing." Afterpulsing occurs when the transmitted cascade of electrons ionizes residual gases inside the PMT, accelerating the ions towards the cathode and generating a secondary pulse that appears after the original photoelectron pulse. The time between the initial signal and the afterpulse is governed by the mass to charge ratio of the ion, and is typically on the order of a few μs.[28] One of Brown University's primary responsibilities within the LUX collaboration is to run dark rate and afterpulsing tests on each PMT that ensure the integrity of the PMT vacuum will hold up in the cold liquid xenon environment.

Ideally, every photon that strikes a PMT will generate a photoelectron and be recorded. In reality, however PMT's have a detection efficiency of approximately 30%. The detection efficiency is a product of two variables: quantum efficiency (QE), and collection efficiency (CE).

1. **QE**: Quantum efficiency is defined as follows:

$$\text{QE} = \frac{\text{\# of photoelectrons produced}}{\text{\# of incident photons}} \tag{2.3}$$

   For an photoelectron to be emitted, an incoming photon must first pass through the glass window of the PMT, get captured on the cathode, and then impart enough energy for an electron to escape into the PMT body. These three actions each have an associated probability that is dependent on the energy of the photon, the material of the cathode and glass, and even the conditions of the external environment. LUX PMT's have a quantum efficiency that is normally distributed with a mean of 33% and a standard deviation of 2.3%.[28]

2. **CE**: Collection efficiency refers to the percentage of electrons emanating from the cathode that strike the first dynode. This value is calculated by comparing the ratio of currents between the anode and the cathode to the total electron multiplication factor. The latter is dependent on the photoelectron striking the first dynode while the former is not, and the ratio between these two measurements yields a CE of about 90%.[28]

After photons are picked up by PMT's, the amplified signals travel through 12m of cable to a set of pre-amplifiers, which linearly magnify the signal 5x more. Then the signal makes its way to a series of post-amplifiers which amplify, shape and output the signals to three different locations to be digitized and filtered. The filtering and organizing of signals saves an immense amount of computer memory and time for

data analysts to work with the information. One basic filter that is applied when deciding which pulses to digitize, is a base threshold below which information coming from the PMT's will not stored. At the end of a very complex processing framework, the information is classified and organized into large data structures accessible in Matlab. For a more in depth description of LUX's data processing setup, see James R. Verbus' [27] or Carlos H. Faham's PhD dissertation [28].

2.2 Background Discrimination

There are many strategies in place to minimize unwanted particles from entering the internal volume of the LUX detector. First and foremost, the detector is located in Lead, South Dakota, a very rural and quiet location. While South Dakota does have snowstorms and hailstorms (even during the summer) that do cause occasional electrical disturbances in the equipment monitoring the health of the detector (not the PMT's), it is not located on a fault line that might cause quakes and geological tremors that could disturb the interior of the experiment. Secondly, the detector is located a mile beneath the surface, shielded from high energy particles streaming to Earth from outer space (of which there are many), as well as any other atmospheric disturbances like storms. Third, the LUX cryostat is surrounded a by a 7.1 m diameter, 6.1 m tall, purified water tank to shield it from radioactivity coming from the Davis Cavern (shown in Figure 2.2b). Within the water tank are 20 Hamamatsu R7081 10" PMT's to detect radiation from any high energy cosmic muons that do manage to make it into the cavern. The data from these PMT's is recorded in tandem with the PMT arrays in the cryostat to veto these events as background radiation. Fourth, all of the materials from which LUX was built went through an involved radiation screening process to minimize the amount of radioactive interference that comes from LUX itself. Finally, liquid xenon is self-shielding, and it protects the inner 300kg active xenon volume from passive detector radiation.

Even with all of these prevention strategies, there are plenty of electromagnetic particles that reach the innermost xenon volume. An important discrimination method to separate electromagnetic recoil (ER) events from NR events like WIMP scatters, is to take the ratio of S2 to S1. Plotting this measurement over a range of S1 values creates two distinct, though slightly overlapping bands known as the ER and NR bands respectively (shown in Figure 2.6a). The discrepancy between the bands arises from the fact that there is a greater rate of recombination in nuclear recoils, which enhances the S1 signal and lowers the S2 signal. Due to the overlap shown in Figure

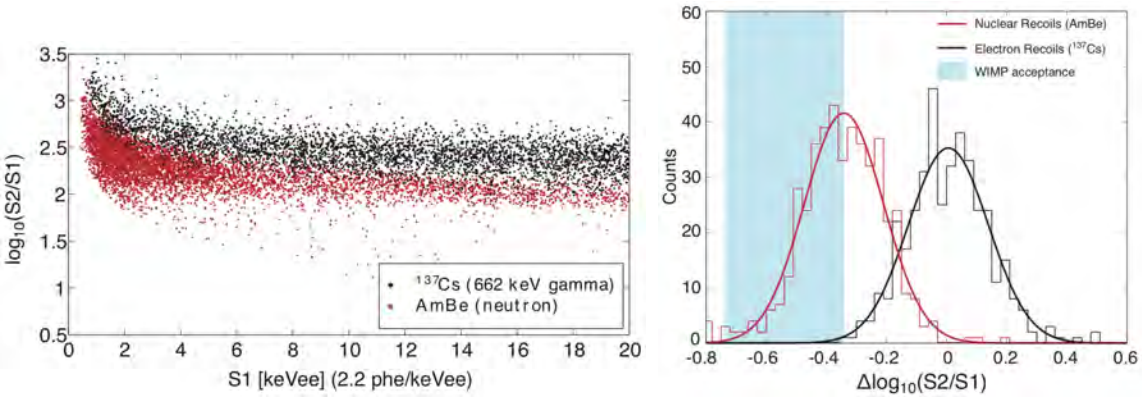

(a) Plot of the ER and NR bands marked in black and red respectively.

(b) Overlaid histograms showing overlap between ER and NR bands, with blue highlighted region to show WIMP acceptance.

Figure 2.6: Visualizations of the ER and NR bands and the overlap between the two.[28]

2.6b, only the lower portion of the NR band is considered in WIMP searches in order to veto 99% of electromagnetic recoils.

Another way to isolate WIMP-like scatters is to recognize that for extremely low cross sections for interaction, the odds that a WIMP would scatter more than once is negligible. Therefore, we can rule out any multiple scatter sites. Beyond this technique and those mentioned above, the best line of defense is to classify as many processes as possible that could create background interference, such as radioactive decay, impurities in the liquid xenon, inelastic captures on detector materials, and even irregularities that may occur farther down the data stream. The better the background discrimination, the more confident one can be that an unaccounted for nuclear recoil is actually from a WIMP.

2.3 D-D Neutron Calibration

One method to calibrate for WIMP-like nuclear recoils is to use neutrons, which are similarly neutral, massive particles, but with a much higher cross section for interaction. Calibrating the detector's response to nuclear recoils is much harder than calibrating electron recoils for several reasons. When calibrating for electron recoils, it is possible to inject a source material that radioactively decays into electromagnetic particles with very specific energies dependent on the reaction. Unfortunately, there is not a convenient monoenergetic neutron source that can be deployed in that manner.

Figure 2.7: A picture of the author standing next to the D-D neutron generator in the Davis Cavern in the summer of 2016.

Additionally, the amount of energy imparted in a nuclear recoil is dependent on the angle of the scatter, which would be difficult to control if a neutron source were located inside the detector. Therefore, the methodology for neutron calibration used in the LUX experiment was to set up a deuterium-deuterium (D-D) neutron generator outside the LUX water tank and install an air-filled collimated tube to transmit the neutrons through the water to the outer surface of the cryostat. The conduit tube itself is 4 m long with a 5 cm diameter.

An Adelphi Technologies Inc. DD108 neutron generator was used to perform the neutron calibration after the 2013 and 2016 LUX WIMP searches. The D-D generator works by ionizing deuterium fuel and accelerating the ions towards a titanium-covered copper target, shaped like a 'V'. The incident deuterium atoms bond with the titanium, then get hit by subsequent deuterium atoms streaming down onto the target, producing He^3 and a neutron (n), outlined by the reaction in Eq. 2.4.

$$H^2 + H^2 \rightarrow He^3 + n \tag{2.4}$$

The neutrons produced by the generator are highly monoenergetic, with energies of 2.45 $\pm$ .05 MeV, and exit the generator in all directions at a tunable rate that

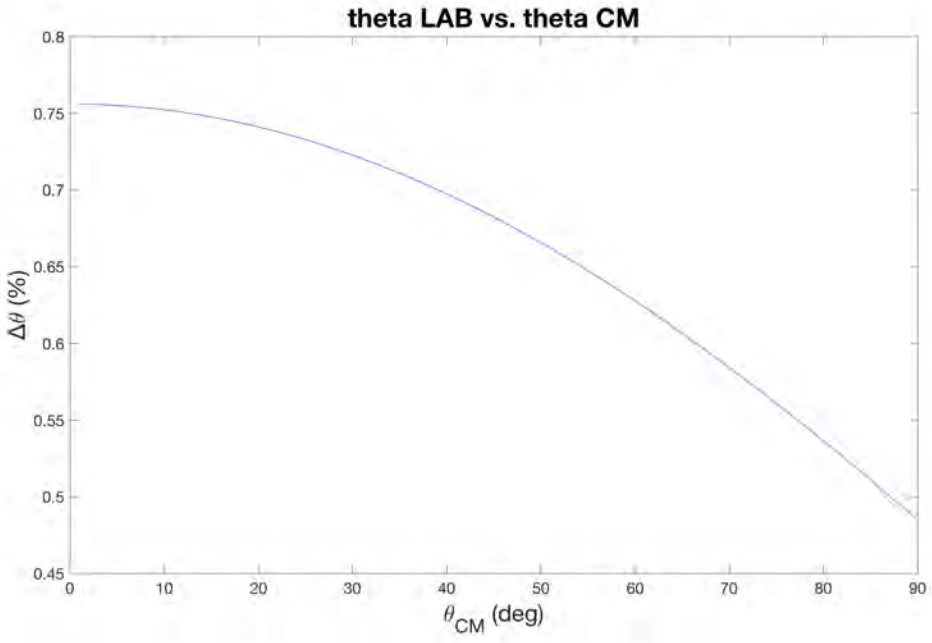

Figure 2.8: The difference between θ_{LAB} and θ_{CM} for neutrons that scatter from Xe in the forward direction. The maximum difference is about .76%. $\Delta\theta = \frac{\theta_{LAB}-\theta_{CM}}{\theta_{CM}} \times 100$

can reach as high as 10^8 neutrons per second. One can also temporally modulate the rate of production by adjusting the ion source and level of ionization with the generator's magnetron. To minimize the radiation hazard to people and electronics alike, shielding was placed around the generator while active. The shielding consisted of a layer of lead, as well as several layers of borated-polyethylene to minimize the neutron flux everywhere save for an opening near the tube(shown in Figure 2.7). A flux of 10^8 neutrons would saturate the LUX detector, so for neutron calibration a flux of 10^6 was used. While this sounds like a large rate, given the random directionality, the distance, and everything in between the neutron generator and LUX, only a small fraction of the neutrons actually make it into the central region of the detector (around 15-20 per second).

As mentioned previously, the angle at which neutrons elastically scatter from a xenon atom determines how much recoil energy is deposited on the xenon nucleus in the interaction. This angle can be measured in the laboratory frame of reference (LAB), but due to the large mass ratio between xenon and neutron, the center of mass (CM) frame of reference can be used as an approximation that greatly simplifies solving for the recoil energy. The CM frame of reference takes the center of mass to be the origin of the coordinate system. Figure 2.8 shows the strength of that approximation for the recoil energy range of interest in this thesis.

The formula that relates the center of mass scattering angle, θ_{CM}, to the recoil energy deposited on the atom, $E_{nr,A}$, is given by Eq. 2.5 below, where E_{in} is the incident neutron energy, and m_n and m_A are the masses of the neutron and the atom respectively. Note that θ_{CM} is defined as the angle between the scattered neutron's altered path and the original line of motion in the CM frame.

$$E_{nr,A} = E_{in}\Big[\frac{4m_n m_A}{(m_n + m_A)^2}\Big]\frac{1 - cos(\theta_{CM})}{2} \tag{2.5}$$

For completeness, the relationship between θ_{LAB} and θ_{CM} is given by Eq. 2.6:

$$\theta_{LAB} = tan^{-1}\Big[\frac{sin(\theta_{CM})}{m_n/m_A + cos(\theta_{CM})}\Big] \tag{2.6}$$

With the position reconstruction capabilities of LUX, one can use the angle between scatters in double scatter events to calculate the recoil energy of the first scatter. This is extremely useful for calibrating light signals coming from nuclear recoils in a given energy range. James Verbus of Brown University performed a calibration for sub 1 keV nuclear recoils using this technique.[27]

2.4 Dark Matter Directionality

As mentioned in Chapter 1, nearly all galaxies appear to have dark matter spread throughout. One viable hypothesis is that the dark matter distribution is in the form of an isotropic, spherical halo, with a Maxwell-Boltzmann velocity distribution that peaks at ∼200 km/s. With this assumption, we can use our expectation for the mass of WIMP's (∼10 GeV/c^2), together with the speed at which our solar system orbits the center of the galaxy (∼230 km/s), to derive the expected flux of WIMP's through the earth. The exact number varies on the hypothesized dark matter distribution and the mass of the WIMP candidate, but a reasonable expectation for the flux is on the order of 10^4 or 10^5 particles/cm^2/s.[29] Due to the motion of the earth around the sun, there is an annular modulation to the dark matter flux. When the earth's orbit is aligned with the direction of the solar system's path of transit through the galaxy, the flux will be greater than when the orbit is in the opposite direction. This modulation is on the order of a few percent, and other forms of direct detection experiments (DAMA/LIBRA for example) are aiming to prove dark matter exists by picking up this signal.

In addition to this annual modulation, the motion of the solar system through the galaxy leads to a preferred direction of WIMP scatters in the detector's frame of

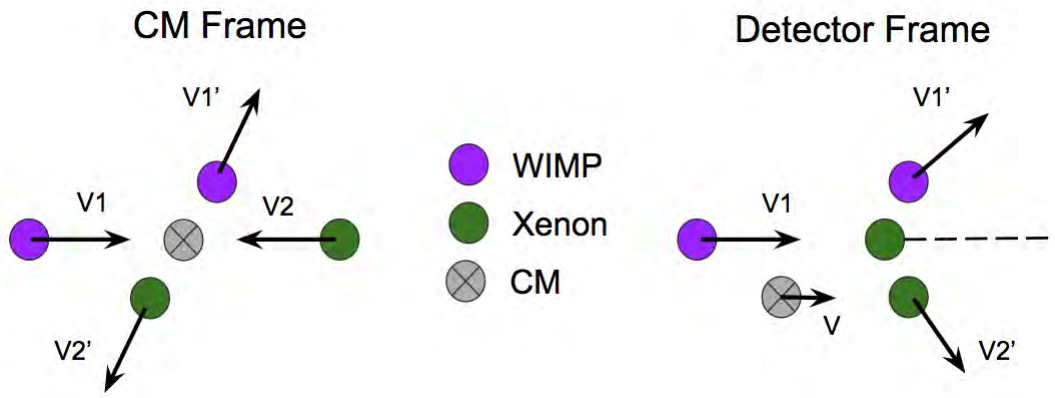

Figure 2.9: A drawing showing how the transition from the isotropic CM scattering frame to the Solar System frame leads to scatters along the axis of incident WIMP's.

reference. Statistical estimates demonstrate that one should expect an order of magnitude more WIMP scatters along the axis of incident direction than perpendicular to the axis of incident direction.[30] This effect is a product of the transition between the galactic frame of reference and the comoving, solar system frame of reference. Summarized in Figure 2.9, WIMP's scatter isotropically in the frame of reference where the center of mass is immobile at the origin. However, when the same scatters are viewed in the solar system frame of reference, the added horizontal component of velocity from the motion of the center of mass results in scattering angles that preferentially converge along the axis of the incident WIMP. Therefore, if we could discern the axial direction of a xenon recoil, we could use that knowledge to better discriminate for WIMP recoils. This discriminatory feature is so powerful because this directional behavior is specific to the precise orientation of the earth, the sun, and the solar system with respect to the dark matter in the galaxy, which rules out background events originating from terrestrial sources. If one were to observe a series of WIMP-like scatters spread out in time with a directionality that is in line with expectation, that would have enough statistical significance to claim the discovery of dark matter.

The issue at present is that no dark matter experiment with a large target mass > 1 kg has the necessary resolution to determine the axial direction in which target nuclei scatter. In noble element scintillators like LUX, the best bet for resolving this feature is if the S2 signal modulated discretely based on the direction of the nuclear recoil. Interestingly, it turns out that we do have a basis for expecting an anisotropy in the S2 signal based on the orientation of the scattered xenon nucleus. The reasoning is closely tied to the level of recombination emission present in the

S2 signal. Liquid xenon is dense, so when a xenon nucleus scatters, it collides with more xenon to form a nuclear recoil track of excited and ionized atoms. The detailed behavior of energy loss by ionization electrons along the nuclear recoil track relative to the applied electric field, may modify the chance of recombination. The chance of recombination should be lower when electrons are lifted from a recoil track into a region of higher effective electric field. The size of the S2 signal would be therefore be dependent on the angle between the xenon nuclear recoil track and the applied electric field in the LUX detector (hence the title of the thesis).

This information gives rise to the following research question:

- Using the rationale above, can we measure a variance in the ionization yield (S2) based on the direction of the xenon recoil track?

The objective of this thesis is to explore this question with the nuclear recoils from a neutron calibration dataset. It is important to note that the size of the expected variance in S2 is also dependent on the length of the xenon nuclear recoil track and the strength of the electric field. Because xenon is heavy, the xenon nuclear recoil track is short (on the order of μm). Therefore, the expected anisotropy may be small, but even if no signal is seen, this measurement could inform the structure of future experiments that intend to resolve this feature. In the words of the late, great, Stephen Hawking:

No one undertakes research in physics with the intention of winning a prize. It is the joy of discovering something no one knew before.

- Stephen Hawking

Chapter 3

Nuclear Recoil Analysis

The dataset used for the analysis in this chapter spans 107.2 live-hours of D-D calibration data collected after LUX's 2013 WIMP search run. In total, over 2 million events were recorded and classified into a data structure for processing in Matlab. The first step in the analysis was to place filters, or cuts on the initial dataset to isolate the events of interest to us. These events had to have the following two fundamental criteria:

- The events must be nuclear recoils involving neutrons from the D-D generator.
- The events must be double scatters, so we can measure the recoil energy and calculate the trajectory of the xenon nucleus.

The code used to distinguish double scatter NR events and calculate their energy was heavily based off of the low-energy nuclear recoil calibration done by James R. Verbus at Brown University in 2016 (see [27]). The recoil energy was calculated by measuring the angle between the two scattering vertices and then substituting that into Eq. 2.5. In accordance with the low-energy nuclear recoil analysis, the following cuts were placed on the initial dataset to ensure the energy purity of the incident neutrons, the credibility of the double scatters, and the scarcity of background interference:

1. Neutron energy purity cuts:
    - *First scatter vertex > 15 cm from the neutron entry point.* This cut eliminates neutrons that lose energy from interactions with the detector material around the conduit/detector junction, thus ensuring the monoenergetic property of the neutron source.

- *First scatter vertex within 2.5 cm radius of the center of the neutron beam center.* This ensures the nuclear recoils are from D-D neutrons coming through the conduit.
- *Both scatter vertices within a detector fiducial radius of 21 cm.* This is to eliminate contamination from sources originating in the outer regions of the xenon body.
- *Electron drift time between 30 and 290 μs.* This cut removes external events from the surface and bottom edges of the liquid xenon volume. Together with the first three energy purity cuts, this ensures that 97% of events have incident energies within 6% of 2.45 MeV.

2. Position Resolution Cuts:

   - *Separation between scattering vertices > 5 cm.* This cut places an upper limit on the position reconstruction uncertainty. Scatters too close together could be improperly ordered due to overlapping uncertainty ranges.
   - *Width of S2 pulse for a single interaction site < 775 ns.* This cut is intended to eliminate multiple scatter vertices that occur at similar heights, resulting in conjoined S2 signals that can be misinterpreted as a single scatter. The 775 ns width comes from simulation results that indicate 99% of true single interaction vertices are accepted while 69% of multiple interaction vertices are rejected.
   - *Second S2 < 1500 phd.* This cut is 95% effective at eliminating scatter vertices that were misordered, and accepts 89% of correctly ordered scatter vertices. 1500 phd corresponds to the expected maximum recoil energy of a forward scatter (36 keV), and thus, with this cut we can rule out back scatters that were misidentified as forward scatters by the LUX detector. The reasoning behind filtering for forward scatters shall be explained shortly.

3. ER rejection:

   - *S1 < 300 phd.* This cut eliminates ER events and accepts > 99% of double scatters.
   - *S2 < 5000 phd.* This cut rejects all 39.6 keV gamma rays from inelastic neutrons scatters on Xe^{129} and accepts > 99% of double scatters.

4. Other cuts:

   - *S2 > 36 phd.* This is the low threshold established for identifying valid S2 events, set by the low number of accidental events that are likely interfere with double scatter identification.
   - *Second S2 > 225 phd.* This cut ensures 90% efficient identification of double scatters for events with no S1 contribution from the first scatter. The cut accepts 70% of double scatters before other cuts are applied.

These strict requirements whittle down the 2 million recorded events to 2544 clean double scatters for further analysis.

3.1 Making the Measurement

The first stage of analysis was to verify the position and direction of the incident neutron beam in order to ensure that the cuts mentioned previously are effective. To do so, single scatter neutron events were isolated and plotted in XY and YZ slices of the detector, shown in Figures 3.1a and 3.1b respectively. From these maps, the neutron beam was determined to have an entry point of (7.1, -23.0, 16.1) cm in LUX coordinates and an exit point of (2.9, 24.2, 17.0) cm. Due to the slight horizontal misalignment of the neutron beam path, it is convenient to create a neutron beam coordinate system, one that is parallel to the neutron beam with the origin at the entry point. The relationship between the LUX coordinate system, x, y, z, and the neutron coordinate system, x', y', z', can be expressed as a linear transformation as shown in Eq. 3.1. Note that z' = z and θ_{rot} in this case is 5.1^o.

$$\begin{bmatrix} x' \\ y' \end{bmatrix} = \begin{bmatrix} cos(\theta_{rot}) & -sin(\theta_{rot}) \\ sin(\theta_{rot}) & cos(\theta_{rot}) \end{bmatrix} \begin{bmatrix} x - 7.1\text{cm} \\ y + 23.0\text{cm} \end{bmatrix} \tag{3.1}$$

To ascertain the direction of the xenon recoil track with respect to the electric field, we need to measure the angle between them, designated ϕ. Similar to the polar angle in spherical coordinates, this angle will vary between 0^o and 180^o, where 0^o corresponds to a xenon recoil track that is directed vertically upward and anti-parallel to the electric field, and 180^o corresponds to a xenon recoil track directed downward, parallel to the electric field. Note that the electric field lines stretch downward, but for physical intuition it is useful to define ϕ in terms of the direction electrons will drift (upward). To calculate ϕ, we can use the neutron recoil to calculate the direction of the xenon recoil. Working in the CM frame, we invoke the conservation of momentum

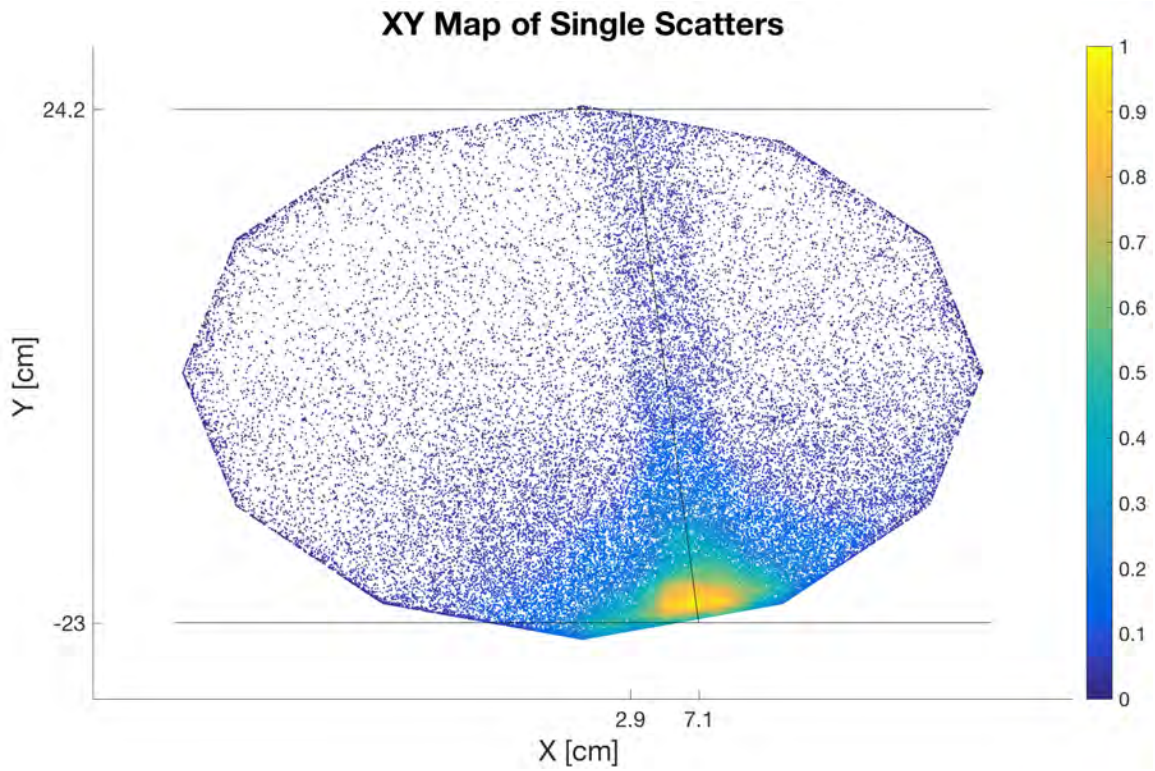

(a) XY map of single scatters in LUX. The horizontal entry point for the neutron beam is (2.9, -23.0) cm and the exit point is (7.1, 24.2) cm.

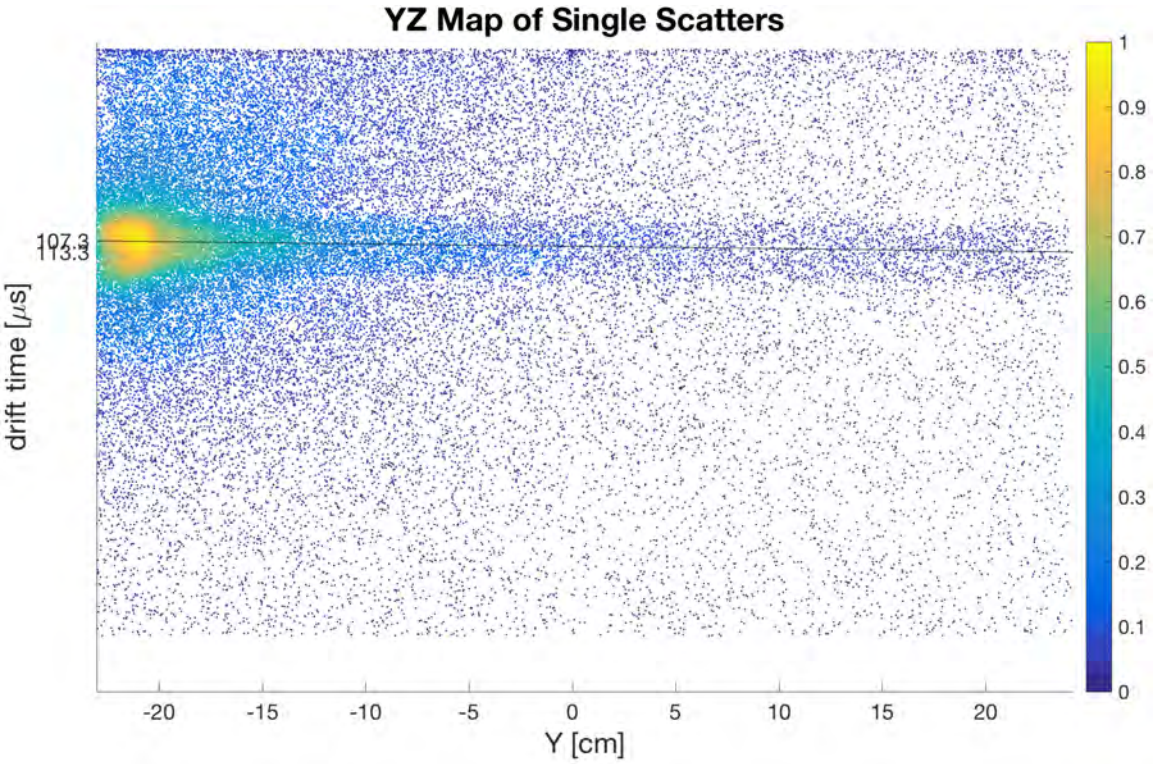

(b) YZ map of single scatters in LUX. The vertical entry point for the neutron beam is at 16.1 cm (107.3 μs) and the exit point is at 17.0 cm (113.3 μs).

Figure 3.1: XY and YZ maps of single scatters in LUX.

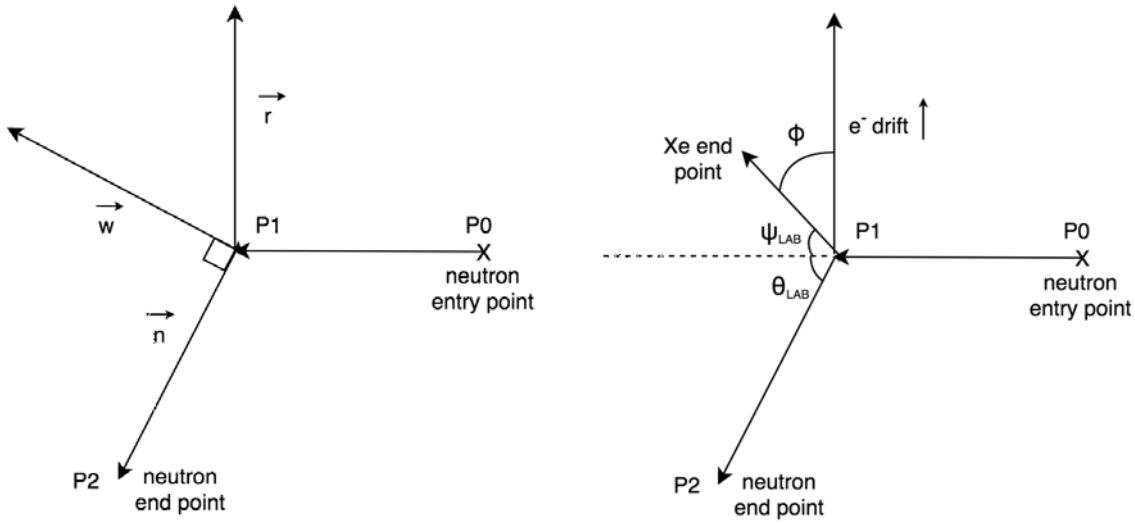

(a) Diagram of the scatter plane coordinate system.

(b) Diagram defining the angles involved in the scattering process.

Figure 3.2: Clarification of the scattering coordinate system and angles.

and traditional kinematics to derive a relationship between θ_{CM} and the angle through which the xenon scatters, denoted ψ_{CM}. This relationship is summarized in Eq. 3.2:

$$\psi_{CM} = \frac{\pi - \theta_{CM}}{2} \tag{3.2}$$

With the understanding that there is a $< 1\%$ difference between θ_{CM} and θ_{LAB}, we can make the approximation that $\psi_{LAB} \approx \psi_{CM}$. We can then obtain the coordinates of the xenon recoil track by rotating the neutron scatter vector in the plane of scattering by the angle $\theta_{LAB} + \psi_{LAB}$, as shown in Figure 3.2b. Eq. 3.3 defines a vector basis for the plane of scattering comprised of three orthogonal vectors, $\vec{n}$, $\vec{w}$, and $\vec{r}$ and their corresponding unit vectors $\hat{n}$, $\hat{w}$, and $\hat{r}$. In Eq. 3.3, the neutron entry point, first scatter position, and second scatter position are denoted $P0$, $P1$, and $P2$ respectively. These angle and vector definitions are visualized in Figure 3.2.

$$\begin{aligned} \vec{n} &= (P2 - P1)\hat{n} \\ \vec{r} &= \big[\vec{n} \times (P1 - P0)\big]\hat{r} \\ \vec{w} &= (\vec{n} \times \vec{r})\hat{w} \end{aligned} \tag{3.3}$$

To obtain the xenon nuclear recoil track orientation in LUX coordinates ($\vec{X}e_{\text{lux}}$), we first write the vector in terms of the scattering plane coordinates ($\vec{X}e_{\text{sc}}$). Then,

to convert $\vec{Xe}_{\text{sc}}$ into LUX coordinates we multiply by the inverse of the LUX-to-scattering plane coordinate transformation matrix. This procedure is outlined in Eq 3.4:

$$\vec{Xe}_{\text{sc}} = \begin{bmatrix} cos(\psi+\theta) \\ sin(\psi+\theta) \\ 0 \end{bmatrix}$$
$$\vec{Xe}_{\text{lux}} = \begin{bmatrix} \hat{n}_x & \hat{n}_y & \hat{n}_z \\ \hat{w}_x & \hat{w}_y & \hat{w}_z \\ \hat{r}_x & \hat{r}_y & \hat{r}_z \end{bmatrix}^{-1} \vec{Xe}_{\text{sc}} \tag{3.4}$$

Finally, to obtain ϕ we can rearrange the dot product formula between $\vec{Xe}_{\text{lux}}$ and the unit vector (0, 0, 1) in LUX coordinates, which points directly upward. Let us call this the $\vec{E}$, as it is anti-parallel to the electric field and sets the orientation of ϕ. Eq. 3.5 specifies how this is formulated:

$$\phi = cos^{-1}\left[\frac{\vec{Xe}_{\text{lux}} \cdot \vec{E}}{|\vec{Xe}_{\text{lux}}||\vec{E}|}\right] \tag{3.5}$$

At this point it is important to note that we can approximate the electric field as vertical in LUX due to extensive modeling carried out in [31]. Additionally, it must be clarified that $\vec{r}$ is not necessarily parallel to $\vec{E}$ as it might seem from Figure 3.2. $\vec{r}$ is perpendicular to the plane of scattering, whereas $\vec{E}$ points to the liquid xenon surface. This will become clear in later visualizations of the neutron scatters.

3.2 Selecting The Energy Range

We are interested in making a comparison between S2 and ϕ, but allowing for the entire range of recoil energies would result in a wide range of expectation values for S2, and would obscure any kind of subtle variation. Therefore, we must select a small, fixed range of nuclear recoil energies over which to draw events from. There are three factors that motivate our choice of energies:

1. The energies must be small enough to allow for a wide range of ϕ values.
2. The energies must be large enough to lengthen the xenon recoil track to where anisotropies might be identifiable.
3. The energies must be large enough to adequately resolve the position of the first scattering vertex.

4. We desire an energy range that maximizes the number density of events.

The reasoning behind the first point is not immediately obvious. It turns out that the neutron scattering angle, θ, places a lower limit on ϕ. This comes from the condition that the momentum, $\vec{p}$, of the nuclear recoil system must be conserved, which means that the net momentum must remain the same before and after the collision. The conservation of momentum in the lab frame is summarized in Eq. 3.6:

$$\begin{aligned} \vec{p} &= m\vec{v} \\ m_n\vec{v}_n &= m_n\vec{v}_n{}' + m_A\vec{v}_A{}' \end{aligned} \tag{3.6}$$

In this case, the initial velocity of the xenon atom is zero and therefore the neutron initially carries all of the system's momentum. If a neutron scarcely scrapes the xenon nucleus, it will retain most of the forward momentum, imparting most of the horizontal momentum to the xenon nucleus, which, as a result, will scatter nearly perpendicularly.[1] If the scattering plane is parallel to the electric field, and the neutron scatters downwards, then the relationship between θ and ϕ_{min} is given by Eq. 3.7:

$$\phi_{min} = \frac{\pi}{2} - \psi = \frac{\theta}{2} \tag{3.7}$$

Subsequently, $\phi_{max} = 180 - \phi_{min}$, and happens when the neutron scatters upwards. At Eq. 3.7 shows, lower θ maximizes the range of ϕ. This effect, together with the fact that the neutron source is perpendicular to the electric field, constrains us to consider forward scatters with lower energies.

The second factor for considering in choosing an energy range is the length of the xenon recoil track. The higher the recoil energy, the longer the recoil track, and if we are constrained to considering forward scatters, a scattering angle of 90^o would yield the best results. This conflicts with what produces the greatest range of ϕ values, and therefore a compromise must be made. The third factor for consideration helps to find that balance.

The third factor to consider is the number density of scatter events as a function of recoil energy. One might expect the number density to be uniform, but this is not the case. To measure exactly how the neutron scattering cross section varies with energy, we ran a simple simulation using the Geant4 simulation software with the

[1] The conservation of momentum is also the reason that scattered xenon and neutron vectors lie a plane.

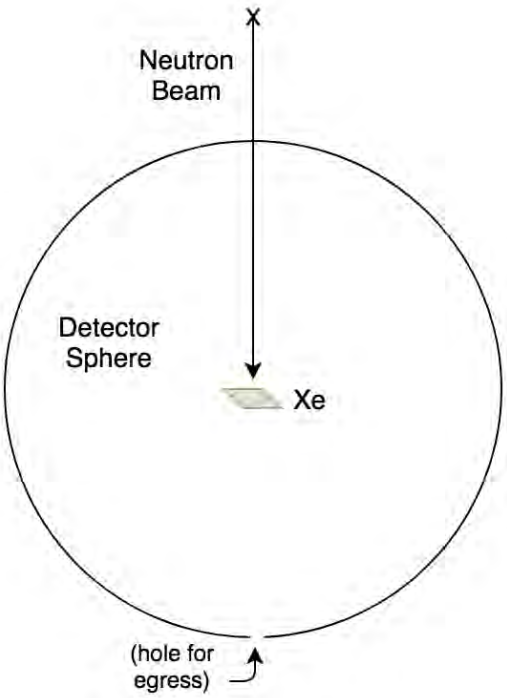

(a) Schematic of neutron energy cross section simulation geometry.

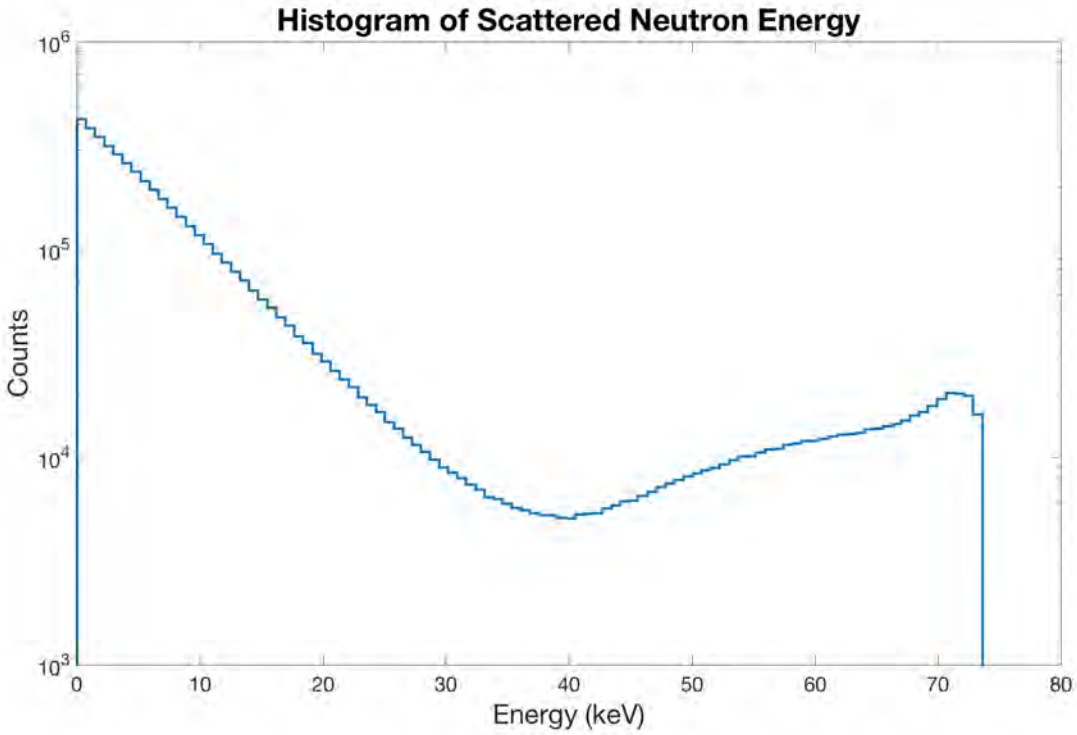

(b) Neutron differential scattering cross section.

Figure 3.3: Neutron scattering cross section simulation and results.

G4NDL3.14 database. The simulation setup involved shooting 2.45 MeV neutrons at a small volume of liquid xenon, and binning the resultant energies. The geometry of the setup is shown in Figure 3.3a. Note that, the xenon volume is several order of magnitudes smaller than the size of the detector sphere, which improves the resolution of the scattering angles. There is also an extremely small egress hole to avoid recording neutrons that do not scatter. To estimate how many neutrons we should run through the small liquid xenon volume to get sufficient statistics, scatters we can do a quick mean free path calculation. The mean free path (l) is the average distance a neutron will travel before scattering in the liquid xenon, and is measured to be 12.6 cm. Described by Eq. 3.8, The initial neutron flux (I_0) exponentially decreases as a function of the distance traveled (x) and the mean free path, leaving I remaining neutrons.

$$\begin{aligned} I &= I_0 \mathrm{e}^{-x/l} \\ P(scatter) &= 1 - \frac{I}{I_0} \end{aligned} \tag{3.8}$$

Therefore, the probability a neutron scatters in the xenon volume is the compliment of the fraction that remain, I/I_0. Given the mean free path of 2.45 MeV neutrons in xenon is 12.6 cm, approximately .79% of incoming neutrons are expected to scatter in the 1 mm of liquid xenon in the simulation geometry. To obtain a smooth distribution, 10^9 neutrons were shot through the geometry, yielding nearly 8 million scatters. After filtering out inelastic scatters, the remaining 5 million neutrons were histogrammed according to their energy and plotted in Figure 3.3b. Figure 3.3b shows that neutrons preferentially scatter forward (at lower scattering angles). This bears relevance to the predicted energy spectrum of WIMP scatters that gives rise to the forward/backward asymmetry, as discussed in Section 2.4.

The scattering angle range $45^o < \theta < 55^o$, was chosen to allow for a large range of ϕ, a longer recoil track, and a high rate of neutron scatters. This angle range corresponds to a recoil energy range of 10.765 keV $< E_{nr} <$ 15.675 keV. Figure 3.4 shows the remaining 126 double scatters after the energy cut was applied.

To obtain estimates for the expected S2 size given the recoil energy, we used the Noble Element Simulation Technique (NEST), an advanced Monte Carlo developed independently by the LUX collaboration to model scintillation processes in liquid xenon.[32] Through this technique, we created an expectation region based on the recoil energy range of the double scatters. Furthermore, using Eq. 3.7 we generated

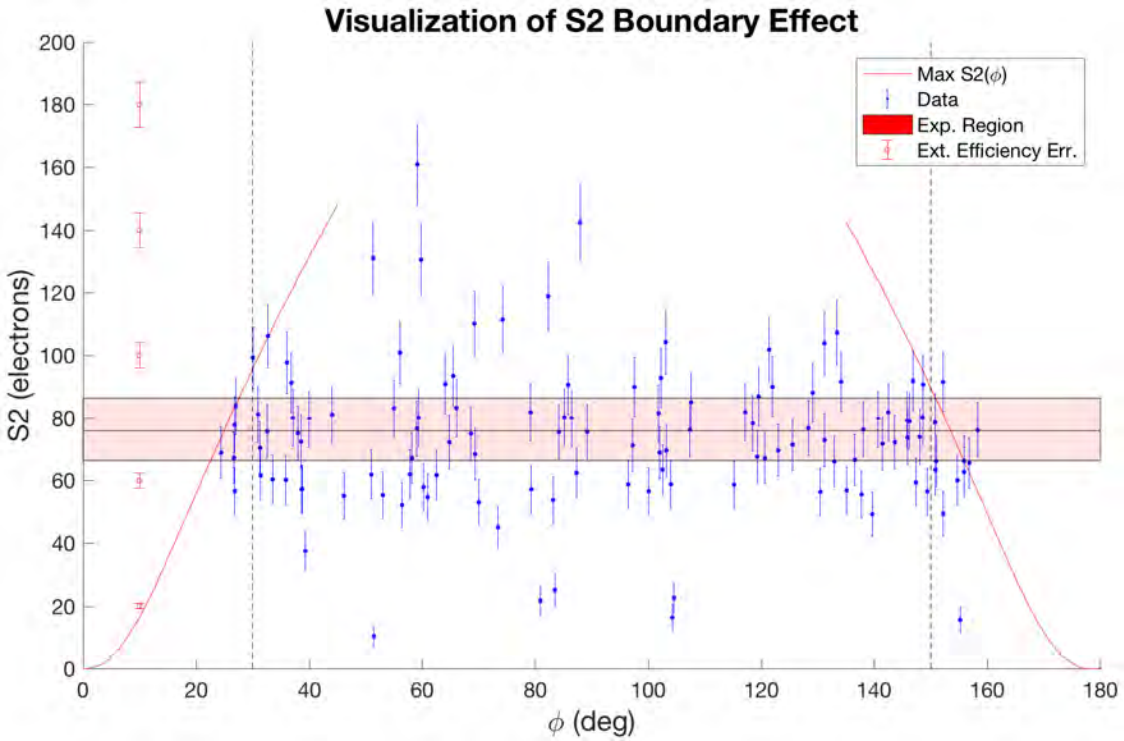

Figure 3.4: Plot showing the S2 bounding effect. The expectation region shown in red corresponds to the anticipated S2 signal size from scatters in the recoil energy range 10.76 to 15.67 keV. The error bars on the data points come from Poisson fluctuation. Also shown on the left-hand side is the global extraction efficiency error of 4%.

upper bounds on the expected S2 size.[2] As one can see in Figure 3.4, these upper limits cut through the expectation range for the S2 size. Because we are looking for a fluctuation about the expectation region, an abnormal absence of data points due to this bounding effect could impede our analysis, and therefore we decided to narrow our range of ϕ values from 30^o to 150^o in order to exclude this unwanted effect from the expectation region.

In order to further reduce the spread in the expected S2 from the differing recoil energies, we choose to normalize the S2 value by the recoil energy, giving us what is commonly referred to in the literature as the ionization yield, Qy (measured in units of electrons/keV). After performing this normalization and applying the ϕ restriction, the final 109 double scatter events passing all cuts are plotted in Figure 3.5. Our first attempt at qualitatively observing a ϕ-dependent fluctuation in Qy was to bin the data in 10^o bins and take the weighted average according to an inverse square weight scheme outlined in Eq. 3.9.

$$\begin{aligned} \langle Qy \rangle &= \frac{\Sigma_i w_i Qy_i}{\Sigma w_i} \\ w_i &= \frac{1}{(\Delta Qy_i)^2} \end{aligned} \tag{3.9}$$

The uncertainty in Qy (ΔQy) comes from two sources of error. The first component is random Poisson fluctuations in the measured S2 signal, therefore the magnitude of the uncertainty scales as the square root of the size ($\Delta S2 = \sqrt{S2}$). The second source of uncertainty is the error associated with measuring the recoil energy. This value is dependent on the position reconstruction uncertainty, and will be derived in full later on.

Referencing Figure 3.5, one can see that there are several low lying Qy points that are much more than three standard deviations (3σ) from the expectation range (circled in red). As a result, the weighted averages are skewed downwards in the corresponding bins, convoluting any possible observed fluctuation. In order to continue analyzing the data, we needed to ascertain where these extreme outliers were coming from.

We came up with several different theories to test:

[2] As an aside, it is important to clarify that the S2 size, as reported in Figure 3.4 and referenced from here on out is the number of electrons ionized at the site of the scatter. This value is obtained by taking the raw S2 measurement in units of phd, dividing by the single electron size (average # of phd per electron), and then dividing by $g2$, the extraction efficiency.

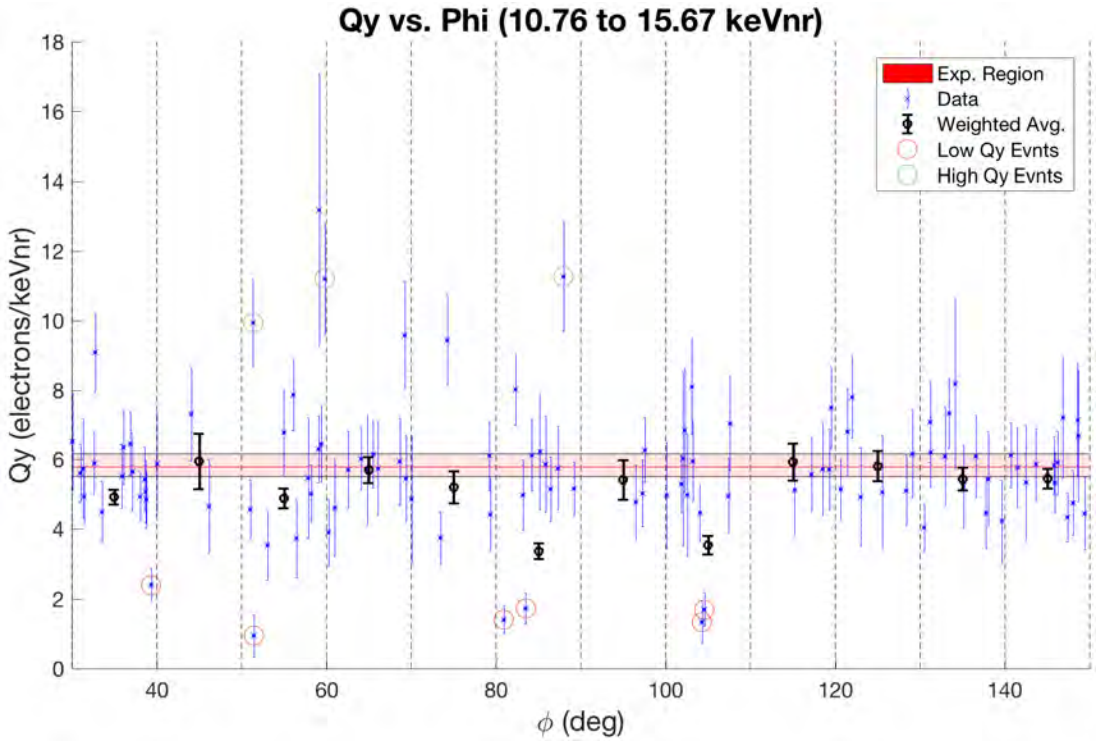

Figure 3.5: A plot of the 109 events passing all cuts. Low outlier Qy events are circled in red, while high outlier Qy events are circled in green. The expectation region corresponds to the recoil energy range of 10.76 to 15.67 keV. The weighted average was calculated from Eq. 3.9, and ΔQy was obtained using the methodology outlined in Eq. 3.13 to Eq. 3.17. Note that ΔQy incorporates the recoil energy uncertainty, which changes the size of the error relative to the expectation region from what it was in Figure 3.4. The global extraction efficiency error is negligible.

1. *Could the scatters have been misordered, and we are actually seeing a lower energy second scatter?* This was largely ruled out after plotting the S2's of the second scatter, as only two of the six events moved within 2σ of the expectation region.

2. *Was there anything apparently anomalous about the digitized set of pulses that might insinuate these are not neutron scatters?* In short, no. There was one event that was caught towards the end of a data capture window that was triggered by an unrelated event, but this could not explain the others.

3. *Are the pulse widths abnormal? This could suggest suggest a contaminated event.* The pulse widths for both the first and second S2 signals were well within range of every other data point in the data set, indicating that these were not coincidental signals of any kind.

4. *Could these events somehow be electromagnetic recoils?* In order to answer this question, we plotted the NR band (referenced in Sec. 2.2), and observed that the ratio of the summed S2 signals to the S1 signals were consistent with nuclear recoils. Interestingly, however, four of the six events had the lowest S1 signals of the data set.

5. *Could the incident neutrons have energies less than 2.45 MeV?* This question arose from the realization that most of the low-valued Qy points had the smallest S1 signals in the data set. Given that the recoil energy of each scatter assumes the incident neutron has 2.45 MeV of energy, a neutron with less energy could have infiltrated the data set by scattering twice with an angle in the range of interest. To estimate the chance of this happening, we ran a simulation using the same Geant4 package but with a modified software that uses intricate LUX geometry called LUXSim. This simulation ran 500,000 neutrons down the collimator tube into the LUX volume. With the help of Graduate Student Casey Rhyne, we applied all the relevant filters to the output and obtained a histogram of the 284 events left after all cuts, plotted in Figure 3.6 [3]

Figure 3.6 shows 7 incident neutrons with energies substantially below the 2.45 MeV mark. This corresponds to approximately 3% of the population, subject to Poisson fluctuation. As a result, this a plausible explanation for the where low-Qy values in the data set come from. These neutrons must have scattered first in

[3]Note that the downsizing of the initial number of events was not as drastic as in the real data from LUX, since the 2 million events from LUX included ER scatters and other background events.

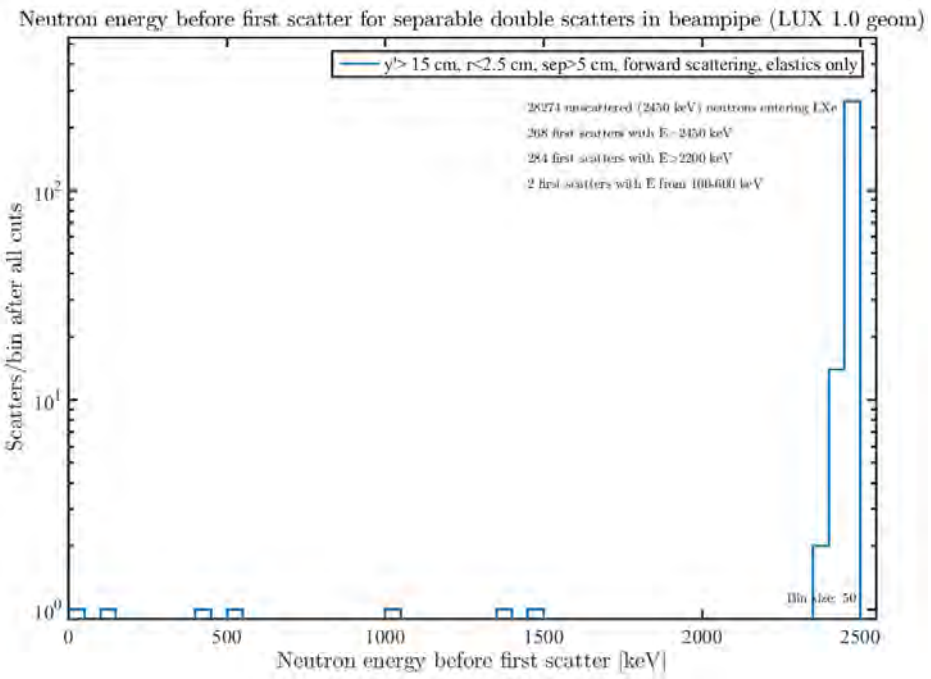

Figure 3.6: A histogram of incident neutron energies demonstrating a low energy tail.

the detector material, and then in the beam pipe, and once more with the desired scattering angle.

In addition to the low lying Qy points, there are several high-valued Qy data points that are $> 3\sigma$ from the expectation region. These events, circled in green in Figure 3.5, were put to the same tests as the low Qy outliers. The scatters did not seem to be misordered, nor was there anything odd about the digitized pulses and widths. While these three events are within the NR band, they appear at the top and towards the higher end of the S1 range. This lead us to question whether the high Qy events might be electromagnetic recoils that made their way into the dataset, since from Figure 2.6 it can be seen that there is a slight overlap between the ER and NR bands at higher S1. However, it is extraordinarily unlikely that these events are electromagnetic recoils due to the very low mean free path of electromagnetic particles in liquid xenon in the energy range of interest. In addition to these hypotheses, the following theories were also discussed:

1. *Could there be two scattering vertices close enough to pass the cut on pulse width?* Doing out the mean free path calculation, there is only a 1% chance of this happening, and therefore that is not the most reasonable explanation for the larger S2 signals.

2. *Is there any cross contamination from scatters close together that pass the 5 cm separation cut?* The separation between two out of the three outlier events is much too great for there to be cross contamination.

3. *Could the excess energy be coming from inelastic neutron scatters?* Inelastic neutrons scatters typically produce energies that are much higher than this energy range, and are cut out by the filters on S1 and S2 sizes.

As of yet, there are no definitive explanations for the excessively high Qy values. We decided that the best way to handle the extraneous points was through a likelihood analysis with a custom probability density function (PDF) that reflects the source of low energy incident neutrons. This analysis is described in detail in the next section.

3.3 Likelihood Analysis

The general methodology behind the likelihood analysis is to obtain a general metric for how likely our data is to have come from a specific probability density function. the PDF should be grounded in physical intuition, and provide a unique likelihood value to each data point based on where it falls in the Qy distribution. The likelihood analysis is similar to a χ^2 diagnostic, but allows us greater flexibility in using non-analytical probability functions and experimenting with different ways to treat the uncertainty and contextualize our data. The goal in performing the likelihood analysis is to test the likelihood of our null hypothesis, (that the PDF has no ϕ dependence) against our alternate hypothesis (that the PDF does have ϕ dependence). Our initial expectation was that our data would be clustered around a constant Qy value in a Gaussian fashion, and we could use a normal distribution to describe the spread of the data. However, due to the presence of what appear to be low energy neutrons, we chose to modify that hypothesis by adding a 3% low-end tail to the PDF, which we shall call a lower tail Gaussian function.[4]

Normal distributions are described by two parameters, the mean (μ) and the standard deviation (σ). To get the best estimates for what those parameters might be for the lower tail Gaussian that describes our Qy data, we first tried to do a simple maximum likelihood estimation (MLE). A MLE explores a parameter space, in this case μ-σ space, to find the parameter combination that maximizes the summed likelihood from all the data points together. Figure 3.7 shows the best fits for three

[4] A Gaussian function is synonymous with a normal distribution.

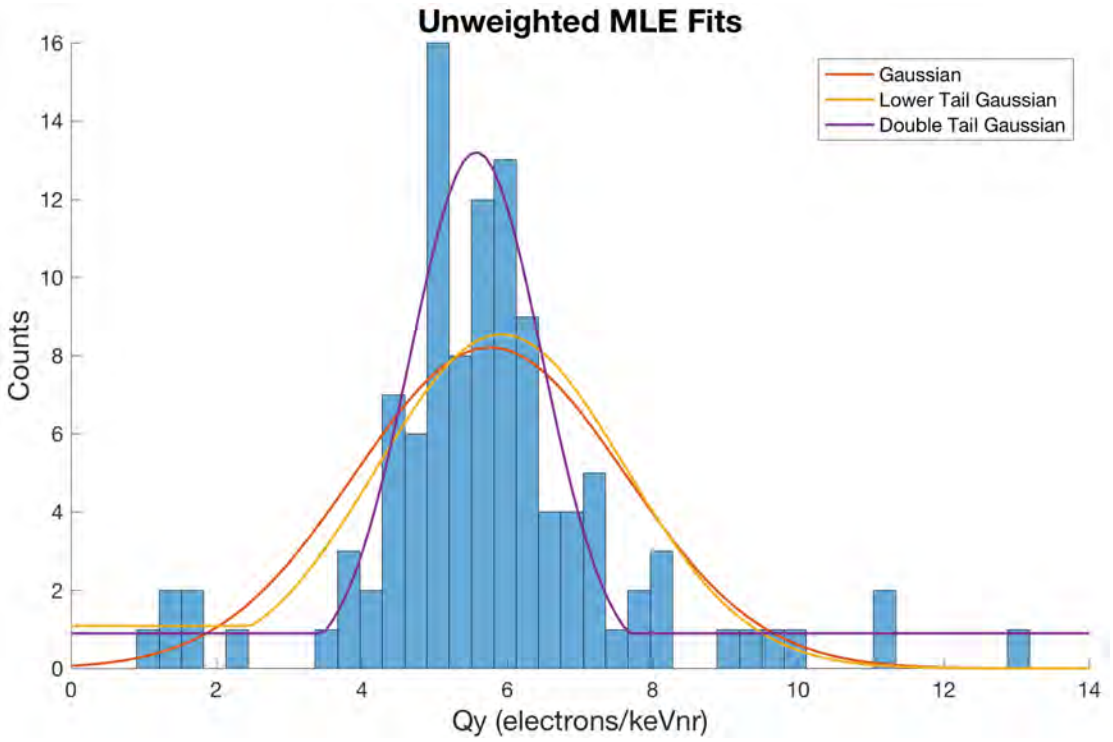

Figure 3.7: A naïve MLE for three different types of Gaussian PDF's.

different Gaussian functions, solely treating the values of the data points themselves and not their associated uncertainty.

It does not come as a surprise that the traditional Gaussian fit is very spread out, since there are outlier events at the low end and the high end of the Qy spectrum. The lower tail Gaussian is also very spread out due to the high-valued Qy points that are a factor of two greater than the expected value, even though their associated uncertainty is large enough to mitigate the egregious gap. The double tail Gaussian fit is notably the best match to the data, but we have no physical basis with which to justify a high Qy tail. Therefore, we decided to pursue the likelihood analysis with the justifiable lower tail Gaussian function.

In order to improve the MLE fit of the lower tail Gaussian, we chose to apply a weight scheme to the likelihood calculation that is inversely proportional to the uncertainty of each point. The purpose of the weight scheme would be to reduce the influence of points with large uncertainty (untrustworthy data). This would ideally reduce the spread of the best fit function by disregarding high outliers with large error. An intriguing way of understanding the effect of the weight scheme is to think of the weights as the number density of data points. The greater the weight, the more data points present in that location. Thus, the likelihood calculation should adhere

to the values that have the greatest density of data points. The specific formula for the weighted likelihood is shown in Eq. 3.10. Note that the likelihood values can often be extremely large or small, and this is suppressed by taking the logarithm of the probability.

$$\mathcal{L} = \Sigma_i w_i Log_{10}(Prob) \tag{3.10}$$

Our initial approach was to use the same inverse square weights as with the weighted average computation. However, when this was implemented, the extremely low Qy values (with proportionally lower uncertainty) had associated weights that dominated the overall likelihood. A review of the literature on the proper methodology for implementing a weighted likelihood analysis led to the conclusion that there is no specific weight scheme that is used. The emphasis on each data point either came from abstract math, i.e. "belief functions," or careful algorithmic work buried in black box statistics functions used to work with particle physics data like RooFit (created by CERN). In the interest of time, two simpler weight schemes will be explored in this thesis that yield tenable likelihood distributions.

3.3.1 Weight Scheme Tradeoffs

The two different weights that were discussed at length were weights of $1/\Delta Qy$ and dimensionless weights equal to $\Delta Qy/Qy$. The rationale behind these two values for the weights was that they both lessened the severity with which the likelihood disproportionately tanked at low Qy. One point of discussion was whether the weights should be unitless or not. One could argue that the weights should incorporate the distance from the expectation region, and therefore scale with Qy. However, one could also posit that the weights should be unitless so that there is no preference for the Qy value itself and all the focus is on the uncertainty. These two options for the weights will affect high Qy values differently. ΔQy increases with the value of the data point due to the Poisson contribution, therefore high Qy values will likely have greater absolute uncertainty than lower Qy values. However, both high and low Qy values may have the same uncertainty relative to the data point itself. Consequentially, the choice of weight will affect these points differently. We do not have an adequate answer as to which weight scheme is best, therefore we shall pursue both weights tangentially throughout the rest of the analysis. The weighted MLE's for both versions of weights are shown in Figure 3.8 along with contour plots that show where the maximum lies in μ-σ space.

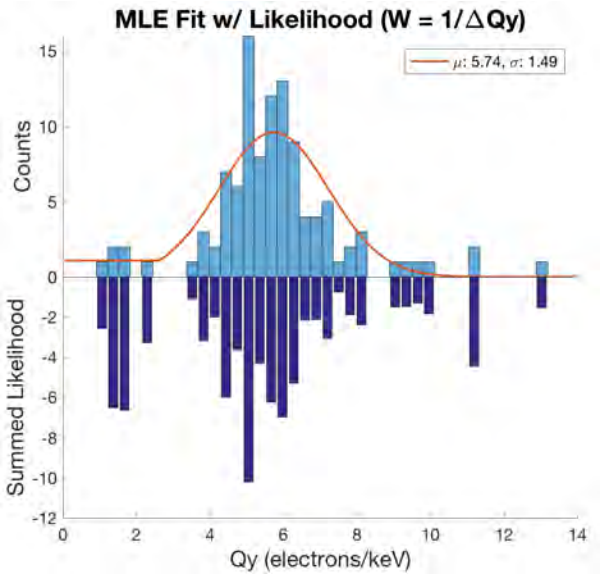

(a) The MLE best fit for weights of $1/\Delta Qy$.

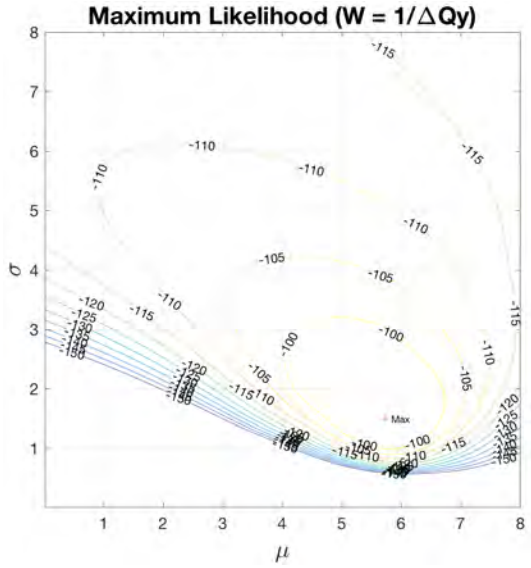

(b) A contour plot showing the location of the maximum likelihood in μ-σ space.

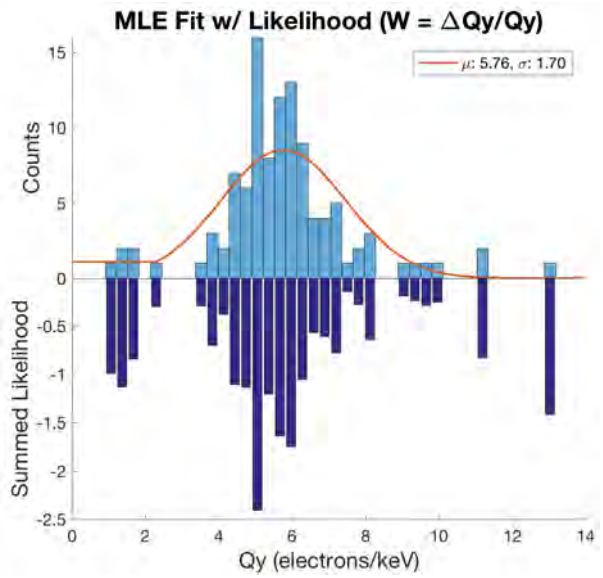

(c) The MLE best fit for weights of $\Delta Qy/Qy$.

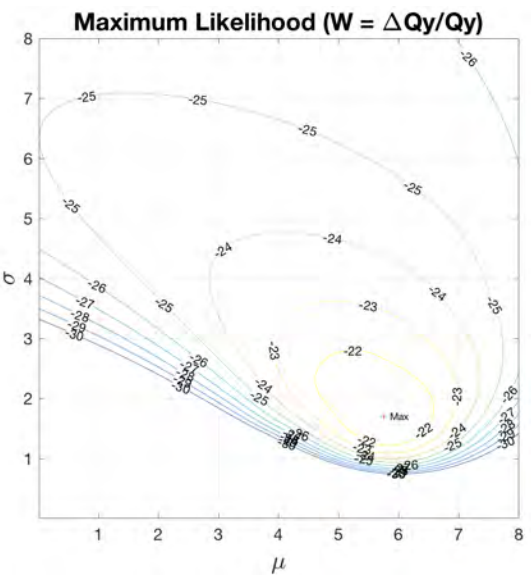

(d) A contour plot showing the location of the maximum likelihood in μ-σ space.

Figure 3.8: Summarizing Visualizations for MLE's of both weight schemes.

Examining the likelihood distribution for weights of $1/\Delta Qy$, the lower tail Gaussian fit appears to be improved from the un-weighted fit shown earlier. One positive aspect of the fit is that the largest Qy data point has a very large uncertainty, and therefore does not drastically impact the summed likelihood. One negative aspect of the fit is that low-valued Qy points are ascribed more weight due to their low uncertainty, and disproportionately lower the likelihood, even though the PDF incorporates a low Qy background prediction. Looking at the $\Delta Qy/Qy$ weight scheme, the PDF has more influence over the weights for high-valued Qy, and the fit is pulled apart by the extrema. It is interesting to see that the low-valued Qy points still appear to contribute a disproportionately negative amount to the overall likelihood in this weighting scheme. This could a product of the incorrectly measured recoil energies, resulting in lower error and higher weights. Overall, each weight scheme has its issues, but they are still an improvement over the un-weighted lower tail Gaussian fit.

Summed log likelihood values of -90 or -21 do not hold any significance in and of themselves. In order to contextualize these likelihoods, one must build a simulation from first principles, and put fake data through the same analysis to obtain a summed likelihood value. By running this simulation thousands of times, we can produce a distribution of summed likelihood, and see where the real dataset falls within this distribution. This is known as "likelihood normalization." The setup and execution of this procedure is covered in the next section.

3.3.2 Likelihood Normalization

To create a random Qy dataset, complete with randomized uncertainty, we need to ultimately obtain the following five variables: S2, ΔS2, E_{nr}, ΔE_{nr}, and ϕ. These variables will come from simulated, randomized double scatters that obey all of the cuts discussed in earlier sections. Creating a Monte Carlo sophisticated enough to do this was non-trivial, and the description of the build process will be broken down into two parts.

3.3.2.1 Part 1: E_{nr}, S2, ΔS2, and ϕ

The first step in generating random Qy values is to sample random recoil energies. We sampled 97% of energies from the 10.76 to 15.67 keV range. The random sampling from this range was informed by the neutron scattering cross section discussed earlier. We fit a log-linear model to the scattering cross section histogram in the relevant energy range, and used that to weight the random sampling. Then, we uniformly sampled 3% of the recoil energies from the 0 to 10.76 keV energy range.

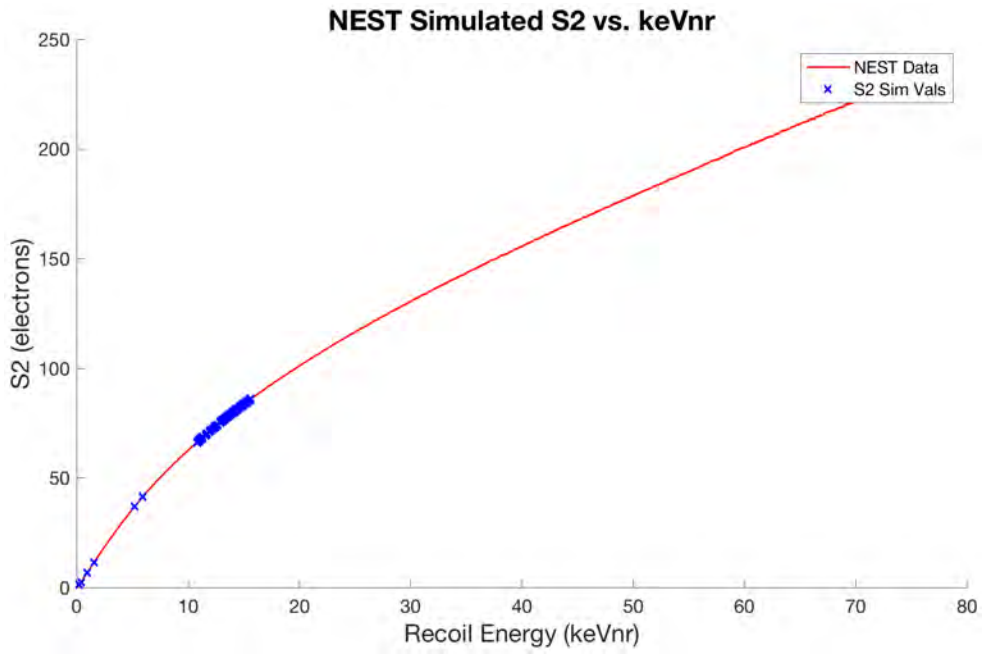

Figure 3.9: NEST model showing relationship between S2 and E_{nr}, as well as a set of randomly sampled points.

To get random S2 values from the recoil energies, a high resolution NEST simulation was used to generate a spectrum of expectation values shown in Figure 3.9. A lookup table was created from the NEST model to match each randomly sampled recoil energy with its expected S2 signal. Note that this approach does not reflect Poisson fluctuations in the S2 signal. This will be addressed later in the Monte Carlo. Figure 3.9 shows that the most random samples are clustered around the intended energy range as expected, with a few events in the low energy region.

ΔS2 can be directly computed as $\sqrt{\text{S2}}$ with the S2 value obtained above. We then randomly sampled ϕ from a uniform distribution between 30^o and 150^o. At this stage, we have all but one random variable: ΔE_{nr}

3.3.2.2 Part 2: ΔE_{nr}

As mentioned previously, ΔE_{nr} is dependent on the reconstruction position uncertainty. The uncertainty for the depth of a collision is constant, but the x,y uncertainty varies with the specific location in the LUX detector. Therefore, in order to complete the faux data set, we need to simulate random scatter positions. Before simulating any scatters, however, we replaced the randomized energies below 10.76 keV with new randomized energies within the valid energy range. Through this method, we

are taking the S2 from a low energy collision, but allowing the neutron to still scatter at angles in the desired energy range, as they do in the real data set.

The first step in creating random double scatters was to choose uniformly random neutron entry positions within a 2.5cm radius around the neutron tube entry coordinates. These were then rotated into the plane perpendicular to the neutron beam path, about an angle of 5.1^o.

To obtain the first scatter position, the neutrons should propagate in the direction of the beam path, adhering to mean free path. Eq. 3.8 was used to develop a PDF from which a distance, D, was sampled, bearing in mind that the distance had to be shorter than the length of the fiducial volume and place the first scatter more than 15 cm into the detector. The height of the first scatter position was taken to be the same as the neutron entry height. To figure out the exact first scatter x,y coordinates, we used the slope (m) of the neutron beam from the entry/exit coordinates, and re-engineered the distance formula to get Eq. 3.11:

$$\begin{aligned} y &= mx \\ x &= \frac{D}{\sqrt{m^2+1}} \end{aligned} \tag{3.11}$$

With the first scatter coordinates in hand, we used Eq. 2.5 to solve for θ based on the random recoil energy. The next step was to obtain the second scatter coordinates given ϕ and θ. This process was very involved. First, we used the mean free path PDF once again to sample a distance the neutron would propagate after scattering, making sure that the separation between scatters was greater than 5 cm and that the second scatter position was not outside of the detector. For a given value of θ, any number of second scatter positions are possible within a cone that emanates from the first scatter vertex. Specifying ϕ then isolates two possible points in that cone where the conditions are met, one in the -x direction and one in the +x direction. Therefore, a 50/50 random chance was applied to determine which direction the neutron would scatter in. In reality this is technically not a 50/50 chance, due to the asymmetrical x-position of the neutron beam in LUX coordinates, but it is a good approximation for the time being.

In order to obtain the specific coordinates of the second scatter, it is best to work in the coordinate system of the neutron beam, x', y', and z'. This is so that we can use a method involving direction cosines. Direction cosines give the position of a vector in a specific coordinate system given the angles between the vector and each

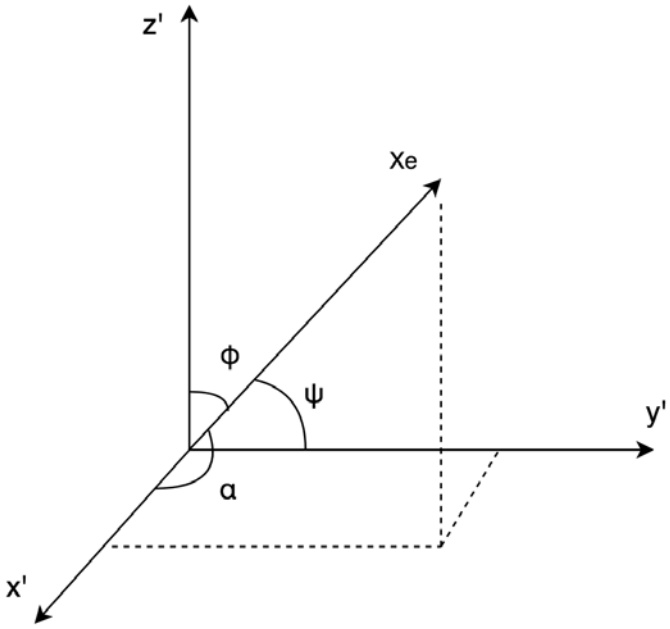

Figure 3.10: A graphic showing the angles referenced in Eq. 3.12.

one of the coordinate axes. Referencing Figure 3.10, we know two of the three axial angles for the recoiling xenon, ϕ and ψ. Therefore, we can use the xenon vector to find the coordinates of the neutron vector, the reverse of the procedure used to calculate ϕ. For our purposes, we shall set the length of the xenon vector, $\vec{Xe}$, to be the propagation distance, D. Solving the system of equations outlined in Eq. 3.12 gives us the coordinates of the xenon vector with length D. We can then transform these coordinates into the LUX frame, and rotate this vector across the scattering plane by $\theta + \psi$ to get the coordinates of the neutron's second scatter.

$$\begin{aligned} cos(\phi) &= \frac{z'}{D} \\ cos(\psi) &= \frac{y'}{D} \\ cos(a) &= \frac{x'}{D} \\ cos^2(\phi) + cos^2(\psi) + cos^2(a) &= 1 \\ D &= \sqrt{x'^2 + y'^2 + z'^2} \end{aligned} \tag{3.12}$$

Now we shall derive ΔE_{nr} in full. ΔE_{nr} is directly dependent on $\Delta\theta$, which, in turn is based on both the position reconstruction uncertainty and the length of the vectors involved. Longer vector lengths will lower $\Delta\theta$ due to the decreased sensitivity of the subtended angle on position shifts. The x-y position reconstruction uncertainties

were obtained through the Mercury algorithm, a LUX specific algorithm that operates similarly to an advanced lookup table. As mentioned previously, the uncertainty in z is constant, and taken to be .1 cm. We can represent each position in terms of its uncertainty, i.e. $\Delta P0 = (\delta P0_x, \delta P0_y, \delta P0_z)$. These position uncertainties are then wrapped into two vectors of error $\Delta V1$ and $\Delta V2$, defined by Eq. 3.13:

$$\begin{aligned} \Delta V1 &= \sqrt{\Delta P1^2 + \Delta P0^2} \\ \Delta V2 &= \sqrt{\Delta P2^2 + \Delta P1^2} \end{aligned} \tag{3.13}$$

The uncertainty in the scattering angle, $\Delta\theta$ is then:

$$\Delta\theta = \sqrt{\left(\Delta V1 \frac{\partial\theta}{\partial V1}\right)^2 + \left(\Delta V2 \frac{\partial\theta}{\partial V2}\right)^2} \tag{3.14}$$

Each $\frac{\partial\theta}{\partial V}$ term is obtained by differentiating Eq. 2.5 and invoking the chain rule and the dot product. The results are presented in Eq. 3.15:

$$\begin{aligned} \frac{\partial\theta}{\partial V1} &= \frac{-1}{\sqrt{1 - \left(\frac{V1\cdot V2}{|V1||V2|}\right)^2}} \left[\frac{V2}{|V1||V2|} - \frac{V1(V1\cdot V2)}{|V1|^3|V2|}\right] \\ \frac{\partial\theta}{\partial V2} &= \frac{-1}{\sqrt{1 - \left(\frac{V1\cdot V2}{|V1||V2|}\right)^2}} \left[\frac{V1}{|V1||V2|} - \frac{V2(V1\cdot V2)}{|V1||V2|^3}\right] \end{aligned} \tag{3.15}$$

The final step is to input $\Delta\theta$ into Eq. 2.5 to obtain ΔE_{nr}. This is shown in Eq. 3.16.

$$\Delta E_{nr} = \sqrt{\left(\frac{2\Delta E_{in} m_n m_A}{(m_n + m_A)^2}\left(1 - cos(\theta)\right)\right)^2 + \left(\frac{2E_{in} m_n m_A}{(m_n + m_A)^2} sin(\theta)\Delta\theta\right)^2} \tag{3.16}$$

Note that in Eq. 3.16, the first part of the contribution to ΔE_{nr} comes from the small uncertainty in the incident energy of the neutrons, ΔE_{in}, which is taken to be .05 MeV. After acquiring ΔE_{nr}, we can finally compute the random uncertainty on Qy, ΔQy, summarized in Eq. 3.17.

$$\Delta Qy = Qy\sqrt{\left(\frac{\Delta S2}{S2}\right)^2 + \left(\frac{\Delta E_{nr}}{E_{nr}}\right)^2} \tag{3.17}$$

With ΔE_{nr} in hand, the last step of the Monte Carlo was to apply random, Gaussian fluctuations to each data point along their uncertainty. The purpose of this

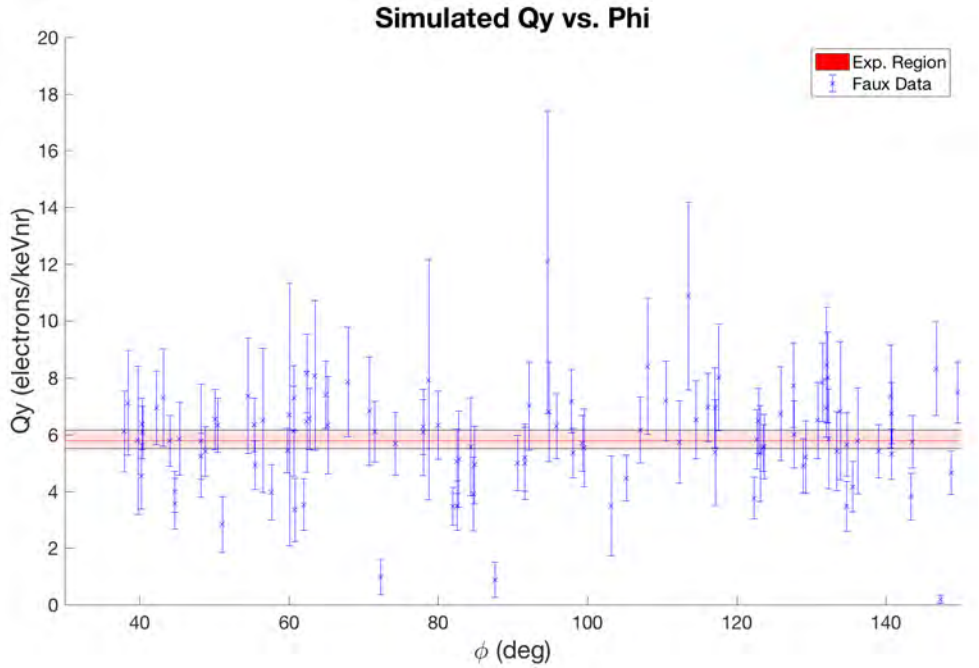

(a) A graphic of the randomized Qy data from the Monte Carlo. As we can see, there are a number of extremely low Qy points as anticipated from the low energy tail, while the rest of the data is clustered around the expectation range with a Gaussian spread.

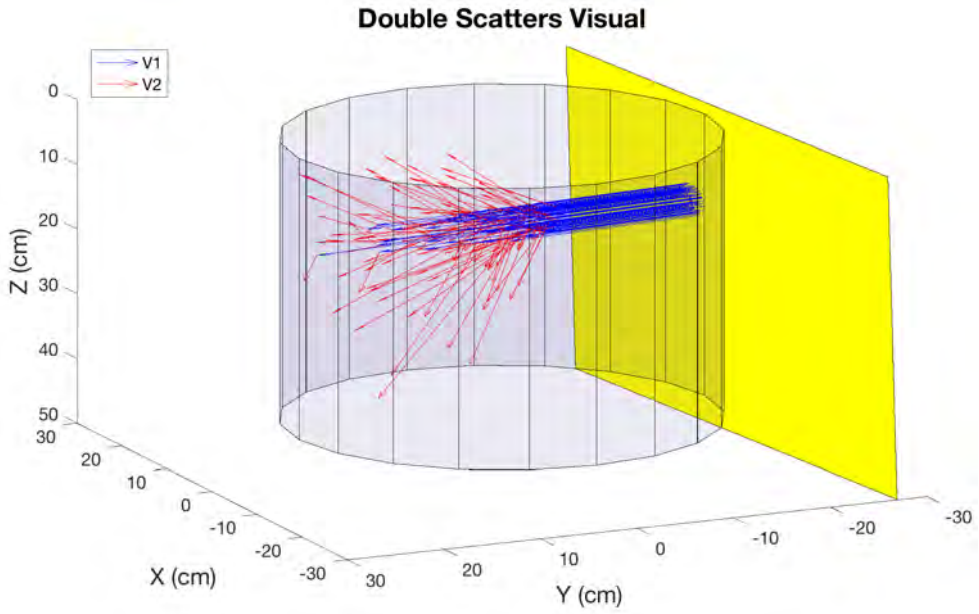

(b) A visualization of the randomized double scatters produced by the Monte Carlo. The blue vectors connect P0 to P1, while the red vectors connect P1 to P2. The fiducial volume is plotted as the grey cylinder, while the plane perpendicular to the neutron beam is shown in yellow.

Figure 3.11: Monte Carlo results.

was to simulate the changes in observed signal size according to error margins. $\Delta S2$ was then adjusted to reflect the Poisson error of the new Qy position. Diagnostics show that the results from the Monte Carlo are relatively consistent with the real data. In particular, the spread of the fake S2 and real S2 signal sizes are very similar. An example of a fake data set created from the Monte Carlo is shown in Figure 3.11, along with a visualization of the scatters in the LUX volume. Furthermore, the likelihood normalizations from running the Monte Carlo 1000 times for each type of likelihood weight are shown in Figure 3.12;

Examining the likelihood normalizations from the Monte Carlo, it is not unreasonable to assume that the real data comes from the hypothesized PDF's. For the $1/\Delta Qy$ weight scheme, it looks as if there's a 15% chance of obtaining data with a worse likelihood than the real data. This value is acceptable. However, it is possible that the Monte Carlo is slightly inaccurate, or that our model is not completely correct. The normalization for the $\Delta Qy/Qy$ weight scheme, on the other hand, shows that the summed likelihood of the real data is better than 95% of simulated data. This is on the borderline of indicating there is a systematic difference. Diagnostics are being carried out to validate the likelihood normalizations.

3.3.3 Hypothesis Test Results

Hearkening back to our initial motivation for comparing S2 with ϕ, we were looking to see if there was a discrepancy between xenon recoils that are parallel vs. perpendicular to the electric field. Parallel scatters would fall closer to 0^o or 180^o ϕ, whereas perpendicular scatters would lie in the 90^o ϕ region. We therefore want to test alternate hypotheses that modify the PDF function in the likelihood calculation to reflect a ϕ dependence. More specifically, we want to shift the μ of the one-tailed Gaussian by some function of ϕ. The three functions that we considered modifying the PDF with were: $Asin(\phi)$, $Acos(\phi)$, and $A\cos(2\phi)$ for an amplitude, A. To implement this alternate hypothesis, we would introduce the amplitude as an extra free parameter and perform a MLE on the real dataset with the alternate PDF forming the basis of the likelihood calculation. If the likelihood of the alternate hypothesis turns out to be an improvement on the null hypothesis (that there is no modulation in ϕ), then we might have wind of an anisotropy.

The test we chose to carry out to determine whether the alternate hypothesis should be accepted over the null hypothesis is the Wilk's ratio test. Outlined in Eq. 3.18, this test takes the ratio of the summed likelihoods of the null and alternate hypotheses (L_0 and L_A), and maps it through the natural log function to yield a value

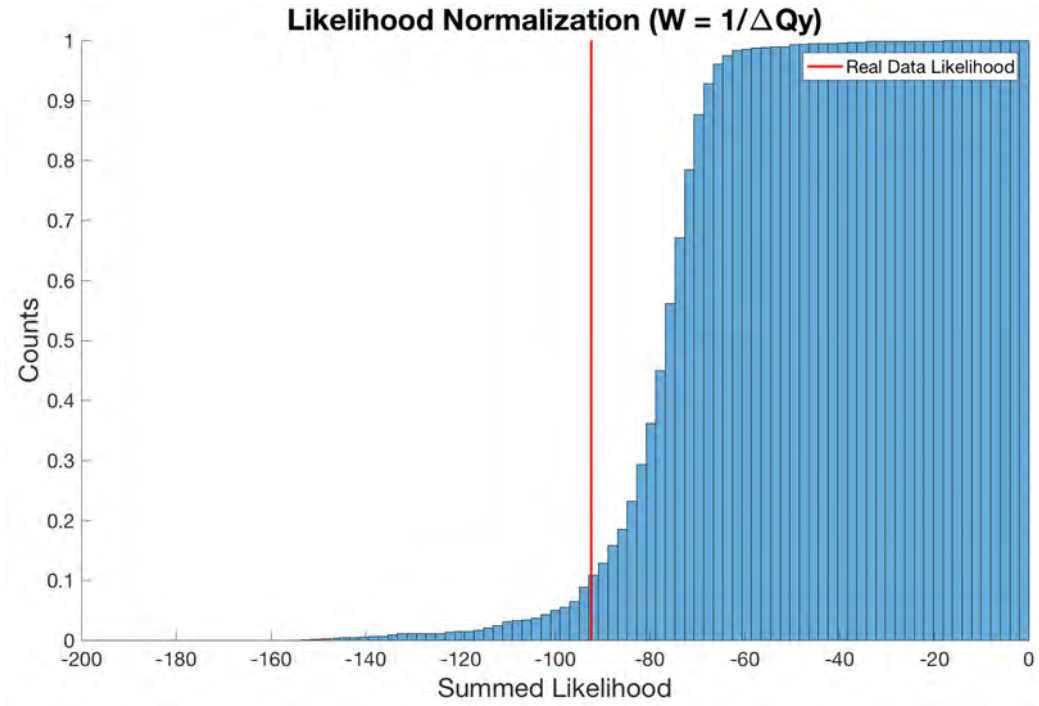

(a) The likelihood normalization for weights of $1/\Delta Qy$. The real data appears at the 15% mark in the cumulative distribution.

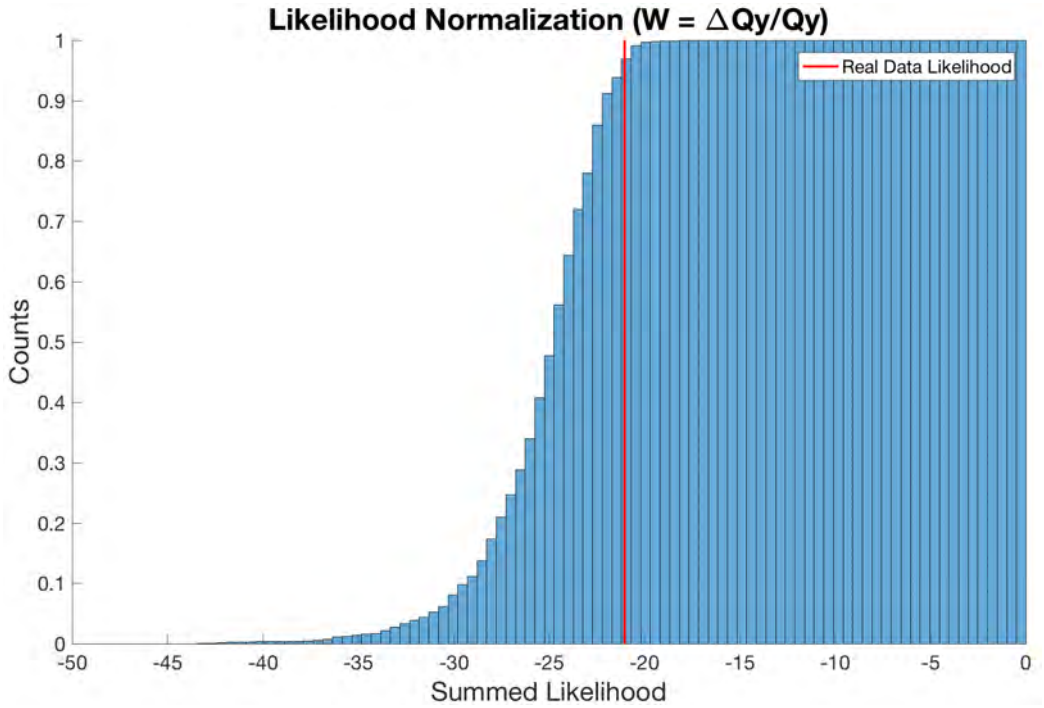

(b) The likelihood normalization for weights of $\Delta Qy/Qy$. The real data appears at the 95% mark in the cumulative distribution.

Figure 3.12: Likelihood normalizations for weights of $1/\Delta Qy$ and $\Delta Qy/Qy$.

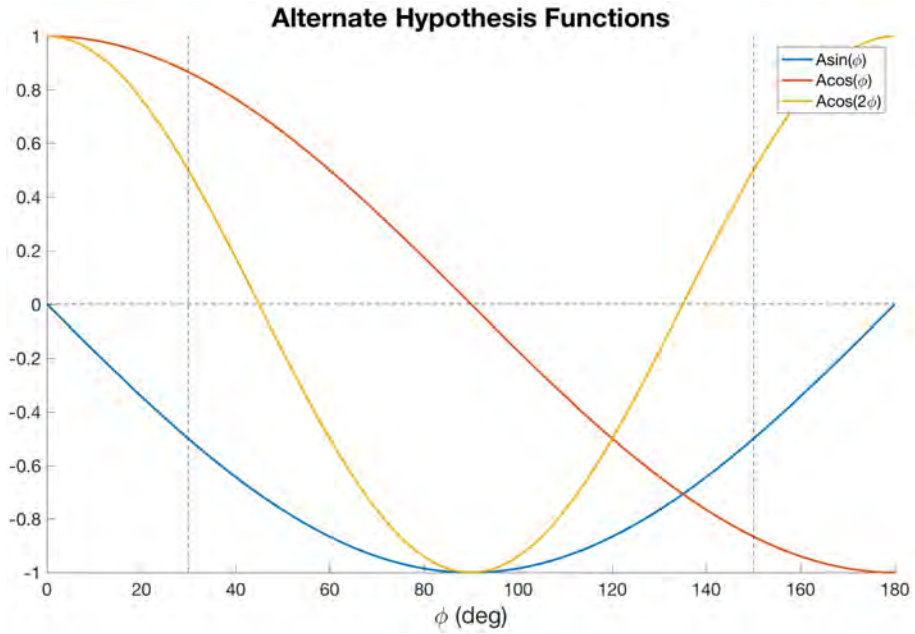

Figure 3.13: Alternate hypothesis functions.

that can be treated as a χ^2 statistic with one degree of freedom. The χ^2 statistic can subsequently be converted into a p-value, and interpreted accordingly.

$$X = -2ln(\frac{L_0}{L_A}) \tag{3.18}$$

The visual results for the MLE's of both weight schemes are shown in Figure 3.14. A summary table of the is included below that contains the chosen ϕ dependent functions that maximized the likelihood and the corresponding p-values from performing the χ^2 diagnostic:

Alternate Hypothesis Summary			
W = $1/\Delta Qy$		W = $\Delta Qy/Qy$	
Function	p-value	Function	p-value
.717sin(ϕ)	.9578	.098sin(ϕ)	.9829
.130cos(ϕ)	.9724	.118cos(ϕ)	.9912
-.228cos(2ϕ)	.9588	-.201cos(2ϕ)	.9685

Before interpreting the results, we carried out several validation tests to give us confidence that they are accurate. Since the $sin(\phi)$ and $cos(2\phi)$ functions have the flexibility to form the same shape, we expect them to converge to the same optimal configuration. We do see this happen in the W = $1/\Delta Qy$ scenario, but there is more of a discrepancy in the W = $\Delta Qy/Qy$ case. This could indicate that the μ-σ-A parameter space has multiple local maxima in the same region. To test this further,

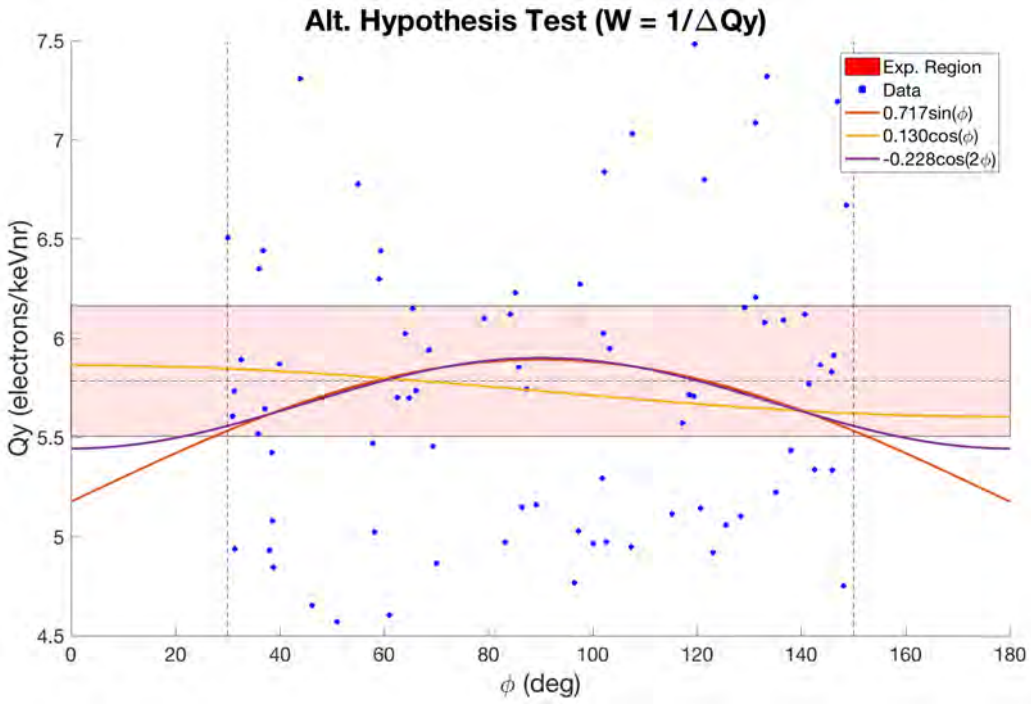

(a) Alternate hypothesis test for weights of $1/\Delta Qy$.

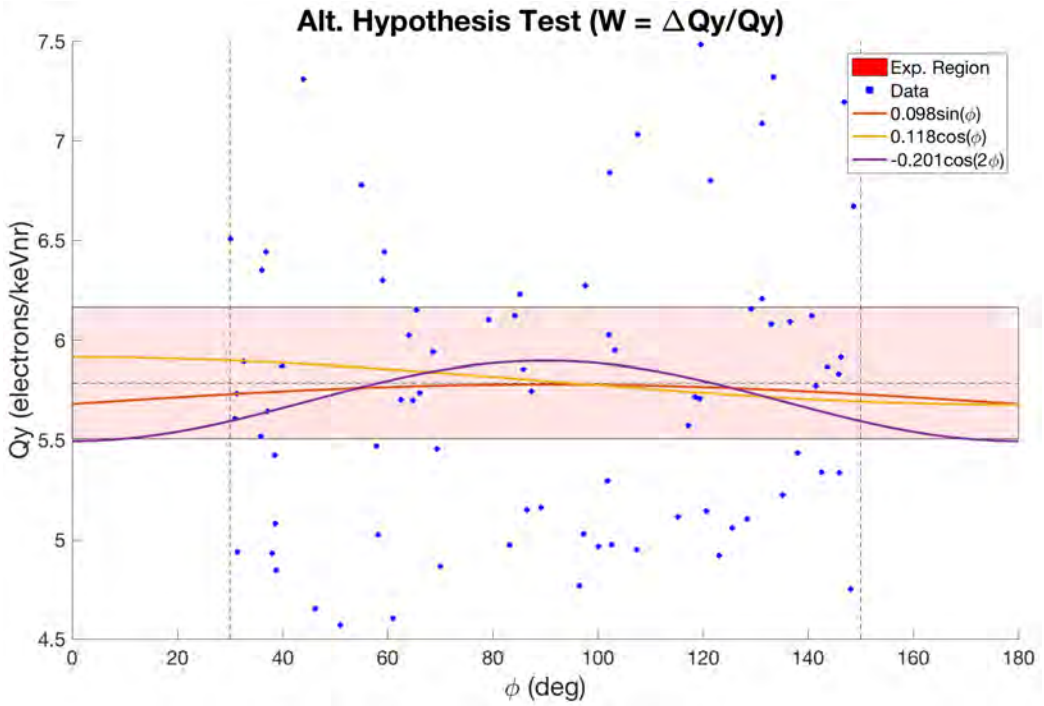

(b) Alternate hypothesis test for weights of $\Delta Qy/Qy$.

Figure 3.14: Alternate Hypothesis Tests

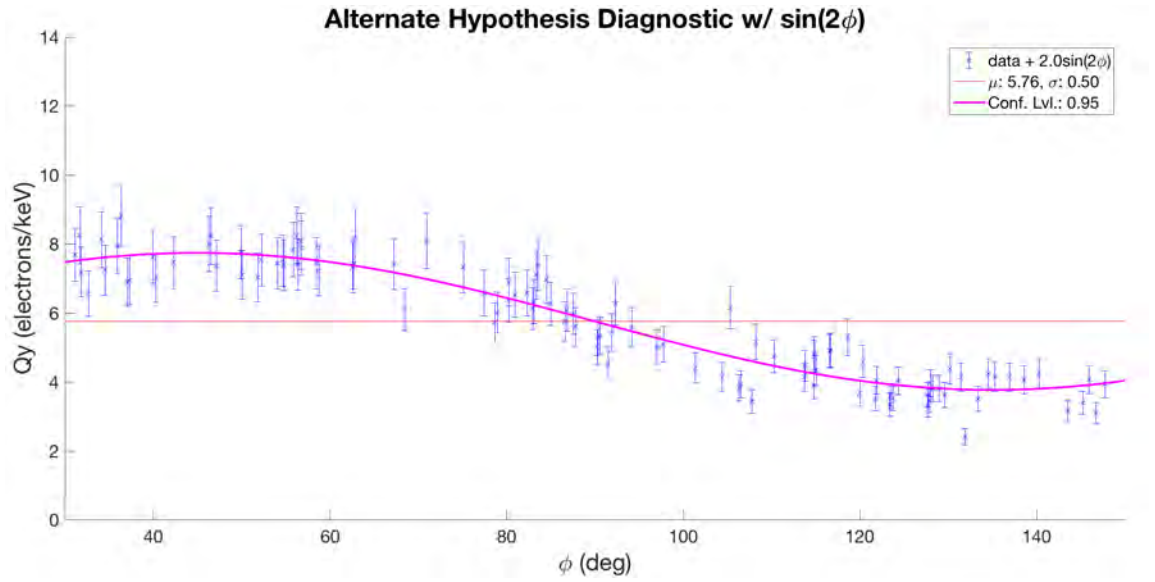

Figure 3.15: Validation that the alternate hypothesis testing code is executed correctly.

we repeated the MLE with various initial positions in parameter space, and looked to see whether they converged. This check demonstrated that there were indeed multiple local maxima due to the relationship between μ and A. An increase in A, counterbalanced by a decrease in μ, resulted in very similar likelihood values that made the final functional form very sensitive to the initial input to the maximization algorithm. One important validation was to pass a fake set of data through the hypothesis testing to see if the code handles it correctly. This was done by generating a series of 100 data points distributed normally about the actual mean value of Qy with a smaller standard deviation of 0.5 electrons/keV. Then, the data was made to vary sinusoidally in ϕ with a sufficiently large amplitude to where the dependence was qualitatively visible. The points were given uniform error that scaled with the size. Running the alternate hypothesis test with the $\Delta Qy/Qy$ weights, the maximization algorithm detected the correct amplitude of the sine function with 95% confidence (p-value of .05), as shown in Figure 3.15

The traditional interpretation of the p-value is that this it represents the percentage of events that are more extreme than the observed data if the null hypothesis is true. In this context, it may be intuitive to think of the p-value as the amount of coincidence between the null and alternate hypotheses. As can be seen from the table above, all of the p-values are above 95%, which indicates that the alternate hypotheses do not markedly improve the summed likelihood of the data.

3.4 Conclusions and Further Work

From the results we can conclude that we did not observe any statistically significant anisotropy in the S2 signal as a function of the angle between the xenon recoil track and the electric field. This could be an important result in and of itself if all other statistical biases are adequately constrained, since we could demonstrate that any existing anisotropy is lower than our sensitivity threshold. However, we have not been able to fully constrain the events in our dataset, due to the fact that there are several events with high Qy that are above 3-σ from the mean. We did find a physical justification for the low Qy outliers, though it is still possible that one of the six identified events could have come from misordering the scattering vertices. In fact, it's possible that one of the events within 1-σ of the mean came from a similar subdominant error. Therefore, the best way in which to improve the analysis would be to get more data, which may be possible from relaxing one or more of the filters placed on the dataset. One cut that could be relaxed is the separation between scatters cut, which was originally put in place to set an upper limit on the recoil energy uncertainty in the low recoil energy analysis. Additionally, we could relax one or more of the neutron energy purity cuts if we accurately modeled the distribution of low energy neutrons with intricate Monte Carlos. Instead of relaxing cuts, it may be possible to use Monte Carlos to explore other aspects of the lower energy scatters that could lead to a cut that would eliminate them from the data set entirely. For example, four of the six low Qy events had the lowest S1 sizes. Perhaps a cut on the minimum S1 size would be beneficial. All in all, there are unaccounted for events in the dataset that impacted the likelihood analysis.

The likelihood analysis seemed to be an effective approach to work with the data, and the alternate hypothesis validation showed that the analysis had ample scrutiny to identify a trend in the simulated data. Even so, the weighted likelihood formulas used in the analysis placed a disproportionate amount of weight on the low-end Qy values. For weights of $1/\Delta Qy$, this is because of the small uncertainty, whereas for weights of $\Delta Qy/Qy$, this arises from high relative uncertainty. Ascribing these data points special treatment under the presumption that they are lower energy recoils is irresponsible. The solution, instead, would be to modify the likelihood formula to treat these points in a rational way, either through modifying the weight scheme, or adding an extra term. The existence of outliers on both ends of the Qy spectrum lead to a PDF function that did not fit the distribution as tightly as it may have otherwise. This could have also resulted in a loss in resolution during the hypothesis

testing. This could also have been reflected in the validation test using simulated data, since there was a clear trend in an ideal dataset, but the confidence level was only 95%. It might be worth testing how the size of the uncertainty in the data affects the p-value. To summarize, future work to improve the results presented in this thesis could involve relaxing cuts to allow for more data, characterizing the outliers, improving the behavior of the likelihood calculation, and exploring the relationship between the uncertainty and the p-value metric.

Particle physics can sometimes seem like whack-a-mole in that attempting to constrain individual particle interactions is extraordinarily difficult. This results in messy data that requires a high standard of statistical rigor to work with it. The benefit to this is that particle astrophysicists develop an expertise in statistical modeling. In particular, the statistics involved in WIMP search analysis is nothing short of amazing. The fact that we have been able to create dark matter experiments at the sensitivity level they are today is also amazing. We are able to isolate and scrutinize the most fundamental constituents of our universe. The next decade will be exhilarating to behold, as direct detection experiments improve, new galaxies are discovered, and more theories get tested. The universe may be expanding but our world is getting smaller.

Bibliography

[1] H. Andernach (translator) and F. Zwicky (author). English and Spanish Translation of Zwicky's (1933) The Redshift of Extragalactic Nebulae. ArXiv e-prints (https://arxiv.org/abs/1711.01693), 11 2017.

[2] Karl Hille. Hubble Reveals Observable Universe Contains 10 Times More Galaxies Than Previously Thought. Web, 10 2016. https://www.nasa.gov/feature/goddard/2016/hubble-reveals-observable-universe-contains-10-times-more-galaxies-than-previously-thought.

[3] P.A.R. Ade, N. Aghanim, et al. Planck 2015 Results. XIII. Cosmological Parameters. *Astronomy & Astrophysics*, 594(A13):1–63, 2016. https://doi.org/10.1051/0004-6361/201525830.

[4] Charles Danforth and Michael Shull. Searching for Baryonic Matter in Intergalactic Space. Web, 2008. http://hubblesite.org/hubble_discoveries/science_year_in_review/pdf/2008/searching_for_baryonic_matter_in_intergalactic_space.pdf.

[5] Alex Harvy. How Einstein Discovered Dark Energy. ArXiv e-prints (https://arxiv.org/abs/1211.6338), 11 2012.

[6] Edwin Hubble. A Relation between Distance and Radial Velocity among Extra-Galactic Nebulae. *Proceedings of the National Academy of Sciences of the United States of America*, 15(3):168–173, 1929. http://adsabs.harvard.edu/abs/1929PNAS...15..168H.

[7] Edmund Bertschinger. Simulations of Structure Formation in the Universe. *Annual Review of Astronomy and Astrophysics*, 36:599–654, 1998. https://doi.org/10.1146/annurev.astro.36.1.599.

[8] Adam G. Reiss et al. Observational Evidence From Supernovae for an Accelerating Universe and a Cosmological Constant. *The Astronomical Journal*, 116(3):1009–1038, 1998.
http://iopscience.iop.org/article/10.1086/300499/meta.

[9] Katherine Freese, Brian Fields, and David Graff. Limits on Stellar Objects as the Dark Matter of Our Halo: Nonbaryonic Dark Matter Seems to be Required. A Part of the Proceedings of the 19th Texas Symposium on Relativistic Astrophysics and Cosmology (https://arxiv.org/abs/astro-ph/9904401), 4 1999.

[10] Roberto D. Peccei. The Strong CP Problem and Axions. *Axions, Lecture Notes in Physics*, 741:3–17, 2008.
https://arxiv.org/abs/hep-ph/0607268.

[11] Michael Schirber. Synopsis: Sterile Neutrino as Dark Matter Candidate. Web, 2014.
https://physics.aps.org/synopsis-for/10.1103/PhysRevLett.112.161303.

[12] G. Jungman, M. Kamionkowski, and K. Griest. Supersymmetric Dark Matter. *Physics Reports*, 267:195–373, 1996.
https://arxiv.org/abs/hep-ph/9506380.

[13] Jonathan Feng. WIMP and Related Miracles. Web, 2009.
http://www.ps.uci.edu/~jlf/research/presentations/0912upenn.pdf.

[14] Tao Han, Zhen Liu, and Shufang Su. Light Neutralino Dark Matter: Direct/Indirect Detection and Collider Searches. *Journal of High Energy Physics*, 2014(93):37, 2014.
https://arxiv.org/abs/1406.1181.

[15] V. C. Rubin, W. K. Jr. Ford, and N. Thonnard. Rotational properties of 21 SC galaxies with a large range of luminosities and radii, from NGC 4605 (R = 4kpc) to UGC 2885 (R = 122 kpc). *Astrophysical Journal, Part 1*, 238:471–487, 1980.
http://adsabs.harvard.edu/abs/1980ApJ...238..471R.

[16] Katherine Garrett and Gintaras Dda. Dark Matter: A Primer. *Advances in Astronomy*, 2011:26, 2010.
https://arxiv.org/abs/1006.2483.

[17] P. Young, J. E. Gunn, J. Kristian, J. B. Oke, and J. A. Westphal. The Double Quasar Q0957 + 561 A, B - A Gravitational Lens Image Formed by a Galaxy at $Z = 0.39$. *Astrophysical Journal, Part 1*, 241:507–520, 1980. http://adsabs.harvard.edu/abs/1980ApJ...241..507Y.

[18] Chris Bon. Event Horizons as the Boundary of the Universe. Web, 2014. http://ffden-2.phys.uaf.edu/webproj/211_fall_2014/Chris_Bon/chris_bon/light.html.

[19] Robert Nemiroff and Jerry Bonnell. A Horseshoe Einstein Ring from Hubble. Web, 2011. https://apod.nasa.gov/apod/ap111221.html.

[20] A. C. Phillips. *The Physics of Stars*. John Wiley & Sons Ltd., West Sussex, England, 1994.

[21] ESA and the Planck Collaboration. Planck CMB. Web, 2013. https://www.esa.int/spaceinimages/Images/2013/03/Planck_CMB.

[22] ESA and the Planck Collaboration. Planck's Power Spectrum of Temperature Fluctuations in the Cosmic Microwave Background. Web, 2013. http://sci.esa.int/planck/51555-planck-power-spectrum-of-temperature-fluctuations-in-the-cosmic-microwave-background/.

[23] Shinji Tsujikawa. Introductory Review of Cosmic Inflation. ArXiv e-print (https://arxiv.org/abs/hep-ph/0304257), 4 2003.

[24] Francis Reddy. Fermi Data Tantalize with New Clues to Dark Matter. Web, 2014. https://phys.org/news/2014-04-fermi-tantalize-clues-dark.html.

[25] Dan Hooper and Tim Linden. The Gamma-Ray Pulsar Population of Globular Clusters: Implications for the GeV Excess. *Journal of Cosmology and Astroparticle Physics*, 8:29, 2016. https://arxiv.org/abs/1606.09250.

[26] D.S. Akerib, S. Alsum, et al. Results from a Search for Dark Matter in the Complete LUX Exposure. *Physical Review Letters*, 118(2):9, 2016. https://arxiv.org/abs/1608.07648.

[27] James R. Verbus. An Absolute Calibration of Sub-1 keV Nuclear Recoils in Liquid Xenon Using D-D Neutron Scattering Kinematics in the LUX Detector (2016). *Physics Theses and Dissertations.* Brown Digital Repository. Brown University Library. https://doi.org/10.7301/Z01G0JQ7.

[28] Carlos H. Faham. Prototype, Surface Commissioning and Photomultiplier Tube Characterization for the Large Underground Xenon (LUX) Direct Dark Matter Search Experiment (2014). *Physics Theses and Dissertations.* Brown Digital Repository. Brown University Library. https://doi.org/10.7301/Z0QV3JV5.

[29] Vitaly Kudryavtsev. Dark Matter and the Universe. Web, 2014. https://www.sheffield.ac.uk/polopoly_fs/1.423787!/file/PHY326-2014-15-dark-matter-and-the-universe.pdf.

[30] B. Morgan, A. M. Green, and N. J. C. Spooner. Directional Statistics for Realistic Weakly Interacting Massive Particle Direct Detection Experiments. *Physical Review D*, 71(10):14, 2005. https://doi.org/10.1103/PhysRevD.71.103507.

[31] D. S. Akerib, S. Alsum, et al. 3D Modeling of Electric Fields in the LUX Detector. ArXiv e-print (https://arxiv.org/pdf/1709.00095.pdf), 8 2017.

[32] M. Szydagis, N. Barry, et al. NEST: A Comprehensive Model for Scintillation Yield in Liquid Xenon. ArXiv e-print (https://arxiv.org/abs/1106.1613), 6 2011.